Theses and Dissertations   1. Thesis and Dissertation Collection, all items

2013-09

The effects of internal tides on acoustic propagation in the Philippine Sea

Coby, Weston R. T.; Fischer, Jacob A.

Monterey, California. Naval Postgraduate School

http://hdl.handle.net/10945/37627

NAVAL
POSTGRADUATE
SCHOOL

MONTEREY, CALIFORNIA

THESIS

THE EFFECTS OF INTERNAL TIDES ON ACOUSTIC PROPAGATION IN THE PHILIPPINE SEA

by

Weston R. T. Coby
Jacob A. Fischer

September 2013

Thesis Advisor: John A. Colosi
Thesis Co-Advisor: Tarun K. Chandrayadula

Approved for public release; distribution is unlimited

THIS PAGE INTENTIONALLY LEFT BLANK

REPORT DOCUMENTATION PAGE

Form Approved OMB No. 0704-0188

Public reporting burden for this collection of information is estimated to average 1 hour per response, including the time for reviewing instruction, searching existing data sources, gathering and maintaining the data needed, and completing and reviewing the collection of information. Send comments regarding this burden estimate or any other aspect of this collection of information, including suggestions for reducing this burden, to Washington headquarters Services, Directorate for Information Operations and Reports, 1215 Jefferson Davis Highway, Suite 1204, Arlington, VA 22202-4302, and to the Office of Management and Budget, Paperwork Reduction Project (0704-0188) Washington DC 20503.

1. AGENCY USE ONLY *(Leave blank)*	2. REPORT DATE September 2013	3. REPORT TYPE AND DATES COVERED Master's Thesis

4. TITLE AND SUBTITLE THE EFFECTS OF INTERNAL TIDES ON ACOUSTIC PROPAGATION IN THE PHILIPPINE SEA	5. FUNDING NUMBERS Office of Naval Research N00014-08-1-0843 and N00014-08-1-0200
6. AUTHOR(S) Weston R. T. Coby and Jacob A. Fischer	

7. PERFORMING ORGANIZATION NAME(S) AND ADDRESS(ES) Naval Postgraduate School Monterey, CA 93943-5000	8. PERFORMING ORGANIZATION REPORT NUMBER

9. SPONSORING /MONITORING AGENCY NAME(S) AND ADDRESS(ES) N/A	10. SPONSORING/MONITORING AGENCY REPORT NUMBER

11. SUPPLEMENTARY NOTES The views expressed in this thesis are those of the author and do not reflect the official policy or position of the Department of Defense or the U.S. Government. IRB Protocol number ____N/A____.

12a. DISTRIBUTION / AVAILABILITY STATEMENT Approved for public release; distribution is unlimited	12b. DISTRIBUTION CODE

13. ABSTRACT (maximum 200 words)

In 2009, a monthlong study was conducted in the Western Philippine Sea. This experiment collected oceanographic and acoustic data from two moorings, the Distributed Vertical Line Array (DVLA) and T1 moorings. The T1 mooring used a 1,095m depth source to send broadband acoustic signals to DVLA receivers located between the depths of 800m and 1,385m. Jacob A. Fischer conducted the internal tide analysis presented in Chapter II. The oceanographic data were used to quantify the characteristics of internal tides in the sample area. Spectral analysis and mode fitting, shows that most of the energy within the internal tides is due to mode 1 of the tidal frequencies. Weston R.T. Coby conducted the acoustic analysis presented in Chapter III. The acoustic data were first used to identify acoustic timefronts across the observed depths, and track the timefronts arrivals. A ray prediction model was then used to match eigenray properties to the observed timefronts. Finally the Viterbi program was used to track timefront arrivals, and intensity for statistical analysis. Weston R.T. Coby and Jacob A. Fischer jointly compared the internal tide and acoustic variability presented in Chapter IV, proving internal tides significantly impact sound speed fluctuations in the Philippine Sea.

14. SUBJECT TERMS Internal Tides, Acoustic Propagation, Philippine Sea, Ray Modeling, Internal Tide Model			15. NUMBER OF PAGES 75
			16. PRICE CODE

17. SECURITY CLASSIFICATION OF REPORT Unclassified	18. SECURITY CLASSIFICATION OF THIS PAGE Unclassified	19. SECURITY CLASSIFICATION OF ABSTRACT Unclassified	20. LIMITATION OF ABSTRACT UU

NSN 7540-01-280-5500

Standard Form 298 (Rev. 2-89)
Prescribed by ANSI Std. 239-18

THIS PAGE INTENTIONALLY LEFT BLANK

THE EFFECTS OF INTERNAL TIDES ON ACOUSTIC PROPAGATION IN THE PHILIPPINE SEA

Weston R.T. Coby
Lieutenant, United States Navy
B.S., Naval Academy, 2007

Jacob A. Fischer
Lieutenant, United States Navy
B.A., Texas A&M University, 2006

Submitted in partial fulfillment of the
requirements for the degree of

MASTER OF SCIENCE IN PHYSICAL OCEANOGRAPHY

from the

NAVAL POSTGRADUATE SCHOOL
September 2013

Authors: Weston R.T. Coby
Jacob A. Fischer

Approved by: John A. Colosi
Thesis Advisor

Tarun K. Chandrayadula
Thesis Co-Advisor

Peter C. Chu
Chair, Department of Oceanography

iii

ABSTRACT

In 2009, a monthlong study was conducted in the Western Philippine Sea. This experiment collected oceanographic and acoustic data from two moorings, the Distributed Vertical Line Array (DVLA) and T1 moorings. The T1 mooring used a 1,095m depth source to send broadband acoustic signals to DVLA receivers located between the depths of 800m and 1,385m. Jacob A. Fischer conducted the internal tide analysis presented in Chapter II. The oceanographic data were used to quantify the characteristics of internal tides in the sample area. Spectral analysis and mode fitting, shows that most of the energy within the internal tides is due to mode 1 of the tidal frequencies. Weston R.T. Coby conducted the acoustic analysis presented in Chapter III. The acoustic data were first used to identify acoustic timefronts across the observed depths, and track the timefronts arrivals. A ray prediction model was then used to match eigenray properties to the observed timefronts. Finally the Viterbi program was used to track timefront arrivals, and intensity for statistical analysis. Weston R.T. Coby and Jacob A. Fischer jointly compared the internal tide and acoustic variability presented in Chapter IV, proving internal tides significantly impact sound speed fluctuations in the Philippine Sea.

THIS PAGE INTENTIONALLY LEFT BLANK

TABLE OF CONTENTS

THIS PAGE INTENTIONALLY LEFT BLANK

LIST OF FIGURES

LIST OF TABLES

THIS PAGE INTENTIONALLY LEFT BLANK

LIST OF ACRONYMS AND ABBREVIATIONS

ADCP	Acoustic Doppler Current Profiler
CTD	conductivity-temperature-depth
DVLA	Distributed Vertical Line Array
GM	Garrett-Munk
NPAL	North Pacific Acoustic Laboratory
ONR	Office of Naval Research
RMS	root mean square
SCA	sound channel axis
SNR	signal-to-noise ratio
STD	standard deviation

THIS PAGE INTENTIONALLY LEFT BLANK

ACKNOWLEDGMENTS

THIS PAGE INTENTIONALLY LEFT BLANK

I.   INTRODUCTION

Weston R.T. Coby, and Jacob A. Fischer jointly prepared the introduction chapter.

A.   NAVAL IMPORTANCE

To maintain the upper hand in the future subsea battle space, the Navy must gain a better understanding of how oceanographic processes affect the ability to detect and identify potential threats. Currently, acoustic detection and resolution methods are favored in the subsea environment. Sound speed perturbations in the ocean medium adversely effect object classification and resolution capabilities. Internal tides are a major source of sound speed perturbations in the open ocean. Identifying and classifying the relationship between sound speed perturbations due to internal tides and acoustic travel times and intensities will allow for future advancements in ocean acoustic technology. Understanding the ocean acoustic variability improves our target identification and detection capabilities.

B.   PHILIPPINE SEA

The Philippine Sea is an oceanographically significant marginal sea in the Pacific Ocean, northeast of the Philippine islands. It is considered one of the most dynamic oceanographic environments in the world, and it is an area that generates very strong internal waves and tides. Several faults and fracture zones border the Philippine Sea, and its basin is host to island chains (Philippine, Marianas, Ryukyu), trenches (Philippine, Mariana) and ridges making it a region of geographical significance (Figure 1).

Figure 1.   Philippine Sea Topographic map showing location of significant features: trenches, archipelago, island chains. From http://mapsof.net/map/philippine-sea-location#.Uf89EVOf9IU

Internal tides are internal waves propagating at tidal frequencies. Internal tides (baroclinic tides) are generated by the barotropic tidal forcing of water over significant bathymetric features. The more significant the bathymetry and barotropic tidal forcing within the region, the more intense the internal tides (Garrett and Kunze 2007). The Philippine Sea is host to several potential generation sites for internal tides due to its complex and rough sea floor. The Luzon Straight in particular is an area known to generate strong internal tides, but their generation at the site is variable (Colosi et al. 2012). Several experiments have been conducted to study the characteristics, and propagation of internal tides in the northern Atlantic, central Pacific, and eastern Pacific, yet few have been conducted in the western Pacific. Figure 2 shows the modeled

displacement (flux) - dominated by mode one- of the internal tides. The significance of the Philippine Sea is best seen in Figure 2 by the relatively large displacements in the northern Philippine Sea as compared to the north central and northeastern Pacific Ocean.
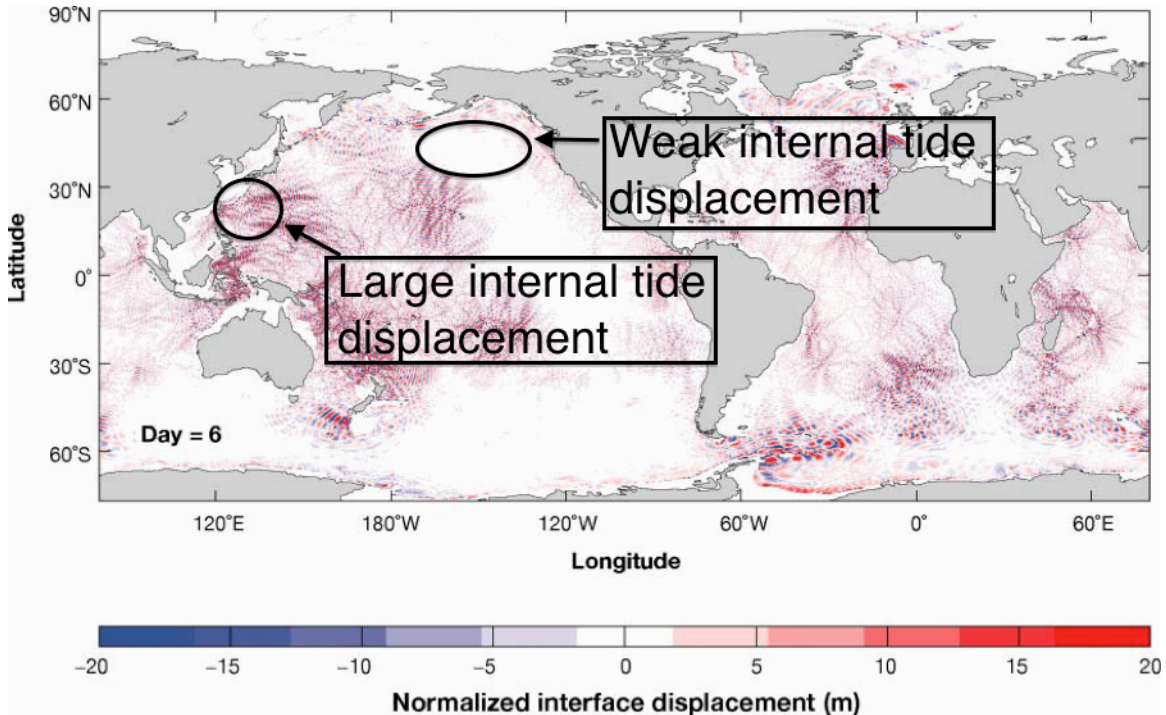
Figure 2.   Shows the propagation of internal tides as measured through displacements (After Garrett and Kunze 2007)

C.   2009 NPAL PHILIPPINE SEA EXPERIMENT

The North Pacific Acoustic Laboratory (NPAL) is a term that was first used to describe a series of acoustic propagation experiments using low frequency broadband sources, and various large aperture vertical and horizontal receiving arrays in the mild (low-level eddy variability) northeast and north central Pacific Ocean from 1989-2005. From these initial experiments, the background sound-speed field, small-scale sound-speed variability due to internal waves, spice, and noise sources were determined (Worcester and Spindel 2005). A second series

of deep-water acoustic experiments were conducted from 2009-2011 in the oceanographically and geologically complex region of the Philippine Sea.
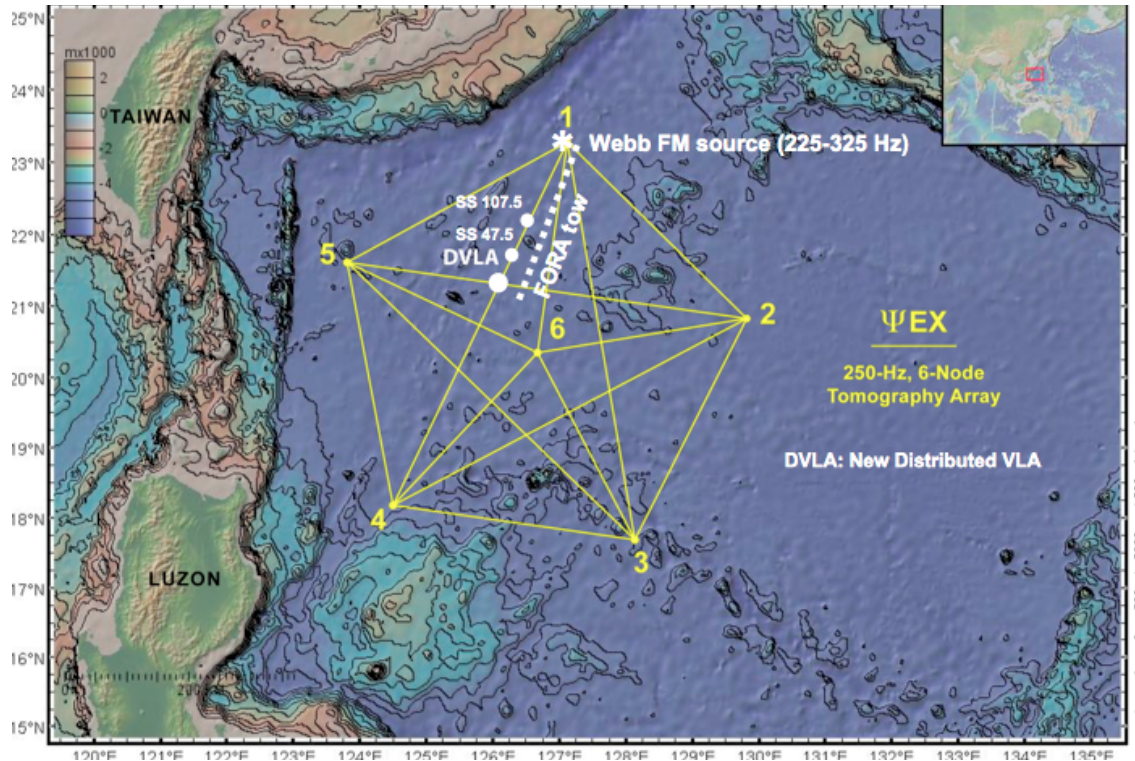
Figure 3. NPAL Philippine Sea Experiment area (From Worcester 2008)

The series of experiments consisted of the NPAL pilot study/engineering test (Spring 2009), NPAL Philippine Sea Experiment (2010-2011), and Ocean Bottom Seismometer Augmentation of the NPAL Philippine Sea Experiment (2010-2011). The Philippine Sea experiments utilized moored and ship suspended low frequency transmitters to send signals to the newly developed Distributed Vertical Line Array (DVLA), acoustic Seagliders, bottom seismometers, and a towed hydrophone array to record the transmissions and ambient noise. Some of the goals of these experiments were to better understand (Worcester 2013):

- The impacts of ocean processes on acoustic propagation.
- The ability to generate a useful ocean model that can aid in improving acoustic predictions.

4

- Scattering, as it relates to spice and internal waves.

- How ambient noise varies in time and space.

- The connection between the seismic field in the seabed and sound propagation in the water column (Worcester 2013).

This thesis focuses on the data collected during the 2009 NPAL pilot study, conducted between April-May 2009, and sponsored by the Office of Naval Research (ONR). The monthlong pilot study was conducted using a single transmitter to test the DVLA in preparation for the follow-on yearlong experiment, which used six transmitters. The pilot study provided initial acoustic observations in the northern Philippine Sea, and verified the proper function of the equipment used in the experiment the following year (Worcester 2008).

During the pilot study acoustic and oceanographic data were collected from two moorings (DVLA and T1) within the region, and from multiple conductivity-temperature-depth (CTD) profiles. Broadband signals were transmitted from the T1 mooring (Number 1 in Figure 3), travelling a horizontal distance of 185 km, to the DVLA mooring (as shown in Figure 3). The NPAL pilot study is unique because this is the first time that scientists have been able to track timefronts throughout the water column in the Philippine Sea. Through the NPAL pilot study and its use of the DVLA, the scientific community is gaining the ability to track and analyze acoustic timefronts throughout the ocean column, in a complex environment to better determine the impact of environmental features such as internal tides on acoustic propagation. The acoustic information gathered required several layers of filtering in order to quantify the physical properties and statistics for each acoustic ray at specific depths. The signal-to-noise ratio (SNR) was calculated from the acoustic data collected in the pilot study, and used to isolate and track the acoustic ray timefronts and the travel time fluctuations over the duration of the experiment. Figure 4 is a plot of the observed timefronts for a single transmission collected from the DVLA receivers. Figure 4 shows the pattern of a wavefront sweeping by the DVLA receivers at a fixed range, displaying the timefront arrival times, and timefront variation with depth. Calculating SNR enabled us to separate the transmission acoustic timefronts

from the background noise (blue background). Tracking the individual timefronts across depth is important because it allows us observe and analyze the evolution of sound rays. The arrival times for the individual timefronts vary significantly with increasing depth as shown by Figure 4.
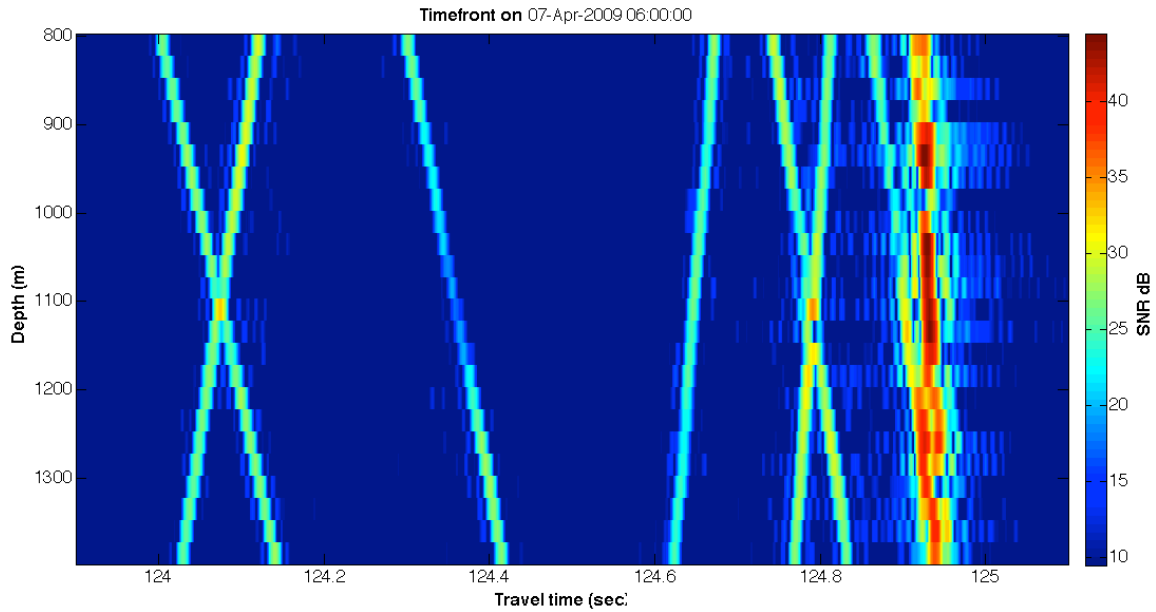
Figure 4. Timefront plot displays the separate eigenray arrival times for DVLA receivers between 800m and 1,385m for a single transmission.

Figure 5 is a plot of the timefront receptions measured at the 1,000m DVLA receiver over the duration of the experiment (y-axis). Since Figure 5 only uses the SNR data from the receiver at 1,000m it shows how individual timefronts vary in time at a fixed depth.
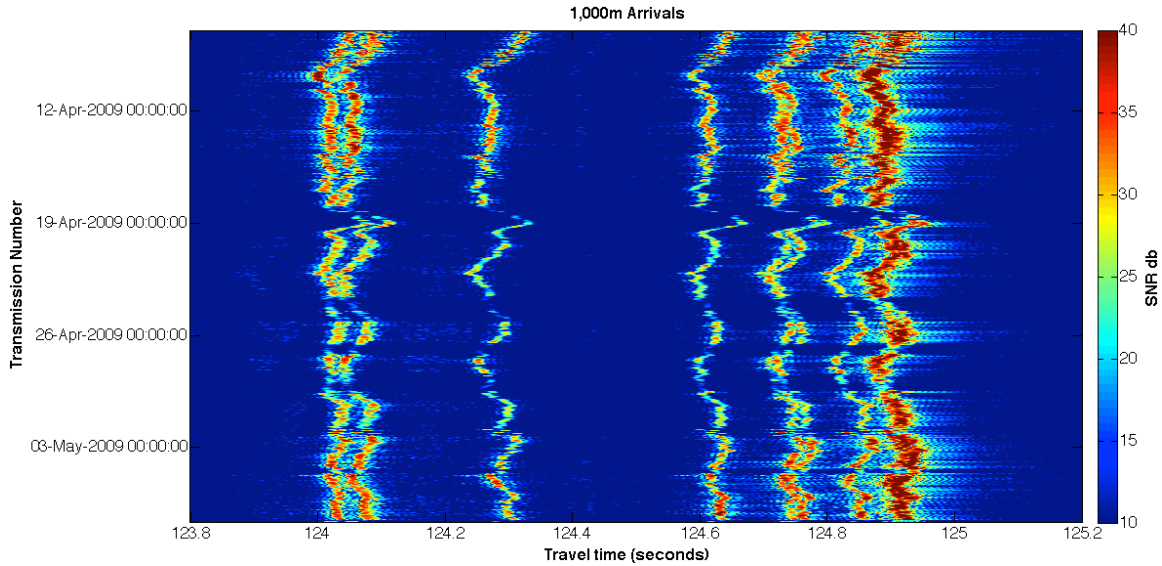
Figure 5.   Time series plot of timefront arrivals at the 1,000m DVLA receiver shows arrival time fluctuations for individual timefronts throughout duration of the pilot study.

Moving on to the oceanographic data, there were temperature, salinity, and pressure measurements taken at both moorings. These data were exploited to track isopycnals (surfaces of constant potential density) and isotherms (surfaces of constant temperature) between 120 and 2,000 meters (Figure 6), and to calculate sound speed fluctuations stemming from internal tides and intrusive oceanic structures.
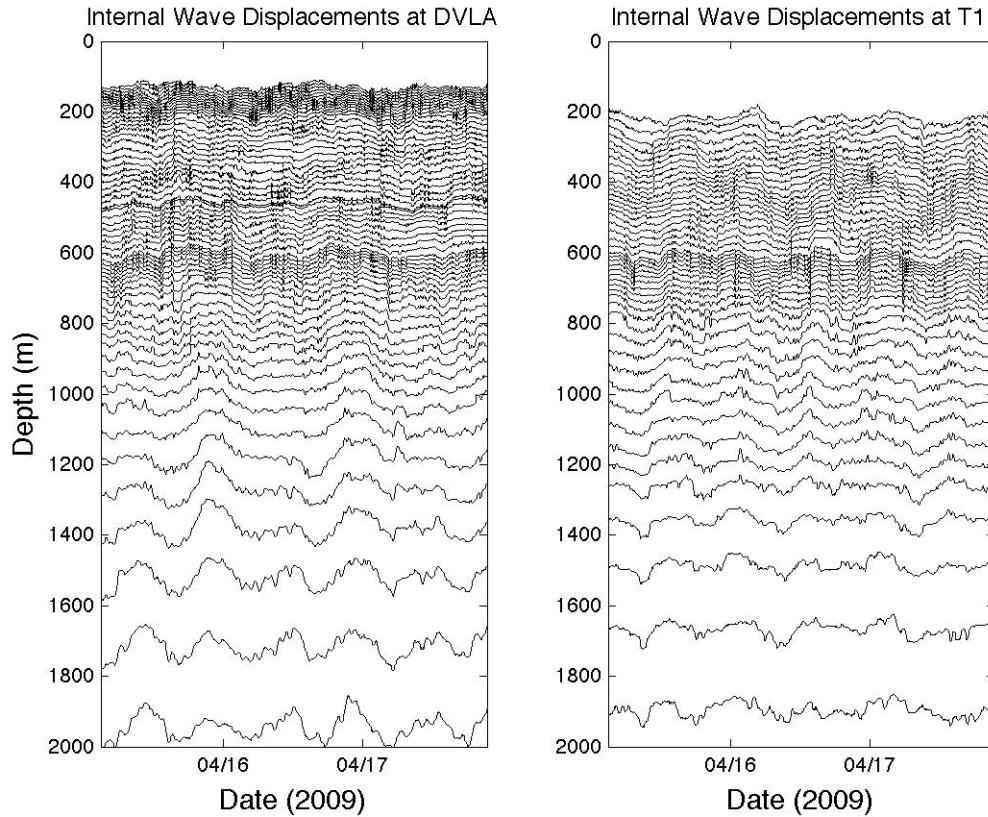
Figure 6.   Time series of internal wave displacement by depth at DVLA and T1. Derived from tracked isopycnals and isotherms (After Colosi et al. *2012).*

Oceanographic variability (Figure 6) and the acoustic variability (Figures 4 and 5) are related to each other by the sound speed changes caused by ocean processes. Of these processes, internal tides and random internal waves contribute the most to sound speed variability. Vertical tidal displacements within the water column cause sound speed variability due to their interaction with acoustic signals propagating through the ocean. As the acoustic signal propagates, parcels of water within the tidal displacements interact with the acoustic signals. These parcels of water are physically different than the parcels of water that they have displaced. The differing physical properties (temperature, salinity, and pressure) of the shifting parcels of water will either slow or speed up the acoustic signals passing through them. The potential sound speed gradient is

8

used in determining sound speed perturbations because it is a good marker of water column stability as it relates to internal tides (Munk et al. 2009). Equation 1.1 is used to relate root mean square (RMS) tidal displacement to sound speed perturbation (Colosi et al. 2012).

$$\delta c = \xi \left(\frac{dc}{dz} \right) p \qquad\qquad (1.1)$$

δc - Sound speed perturbation
ξ - Vertical displacement (RMS)
$\left(\dfrac{dc}{dz} \right) p$ - Potential sound speed gradient

The Garrett-Munk (GM) spectrum describes the random internal gravity wave field (Munk 1980). The GM spectrum is significant because it discovered a frequency-wavenumber distribution for internal waves that appeared to be "universal" in space and time, and is "often used as a representative statistical description of the internal wave field (Levine, 2002, p. 3166)." Diurnal and semidiurnal internal tides which are not included in the GM model show energy levels which are approximately equal to those of random internal waves. The random internal wave energy measurements at the T1 and DVLA moorings were relatively constant, so the diurnal and semidiurnal internal tides were separated by their energy fluxes at tidal frequencies (Colosi et al. 2012).

D.   PURPOSE

The analysis presented in this thesis serves to address three main areas: [1] characteristics of observed internal tides, [2] acoustic variability occurring at tidal frequencies, and [3] correspondence between moored observations of internal tides and tidal acoustic variability. This thesis seeks to enhance our understanding of the subsea environment and to improve our understanding of how oceanographic processes influence visibility in the sub-sea battle space.

THIS PAGE INTENTIONALLY LEFT BLANK

II.   INTERNAL TIDE ANALYSIS

Jacob A. Fischer conducted the internal tide analysis presented in this chapter.

A.   LINEAR WAVE THEORY: EQUATIONS OF MOTION AND MODES

In deriving the equations of motion (Equations 2.1-2.3, 2.6, 2.7), we assumed the ocean to be an incompressible fluid and used the Boussinesq approximation; assuming that changes in density throughout the water column were negligible except as they related to terms associated with the force of gravity. (Stewart 2013).

$$\frac{\partial u}{\partial t} - fv = -\frac{1}{\rho_0}\frac{\partial p}{\partial x} \tag{2.1}$$

$$\frac{\partial v}{\partial t} + fu = -\frac{1}{\rho_0}\frac{\partial p}{\partial y} \tag{2.2}$$

$$\frac{\partial w}{\partial t} = -\frac{1}{\rho_0}\frac{\partial p}{\partial z} - g\frac{\rho}{\rho_0} \tag{2.3}$$

The first three equations of motion (Equations 2.1-2.3), the momentum equations, stem from Newton's second law of motion, which governs the response of a parcel of fluid's momentum as a result of forces acting on it; those forces being pressure p, the Coriolis force f, and gravity g. Thinking about the ocean in terms of a Cartesian coordinate system, we get forces acting on a fluid parcel and the resulting motion in three-dimensional space. The three-dimensional space, with respect to the ocean, is broken down into three directions of motion and their velocity counterparts. The east/west direction and velocity are defined by x and u, north/south by y and v, and depth by z and w. Within the $x-y$ plane, forces governing the momentum of the fluid are predominantly pressures acting on the fluid (p) and the force exerted as a result of earth's rotation, the Coriolis force (f).

11

In order to arrive at Equation 2.6, we needed to apply the continuity equation (Equation 2.4) and the incompressibility relation (Equation 2.5). The Buoyancy frequency squared N^2 is equal to $\dfrac{g}{\rho}\dfrac{\partial \rho}{\partial z}$.

$$\frac{\partial \rho}{\partial t} + \bar{u} \cdot \nabla \rho + \rho \bar{\nabla} \cdot \bar{u} = 0 \qquad (2.4)$$

$$\bar{\nabla} \cdot \bar{u} = 0 \qquad (2.5)$$

$$\frac{\partial}{\partial t}\left(g \frac{\rho}{\rho_0} \right) = wN^2 \qquad (2.6)$$

From the principles behind the conservation of mass, for a parcel of water moving within a fluid at velocities significantly less than the speed of sound, the density (mass/volume) is assumed to be a constant value. So, if the density doesn't change, i.e. the particle does not expand or contract, the divergence of the velocity vector field must be equal to zero. This is the concept behind the incompressibility relation (Equation 2.7) (Stewart 2013).

$$\frac{\partial u}{\partial x} + \frac{\partial v}{\partial y} + \frac{\partial w}{\partial z} = 0 \qquad (2.7)$$

The equations of motion were used to derive the linear internal wave equation for vertical displacement $\xi(r,t)$ (Equation 2.8). Important information for the wave equation is the local Coriolis parameter f and the buoyancy frequency profile N(z). Figure 7 shows the N(z) profile obtained from the NPAL pilot study.

$$\left[\left(\frac{\partial^2}{\partial t^2} + N^2 \right)\left(\frac{\partial^2}{\partial x^2} + \frac{\partial^2}{\partial y^2} \right) + \left(\frac{\partial^2}{\partial t^2} + f^2 \right)\frac{\partial^2}{\partial z^2} \right]\xi(r,t) = 0 \qquad (2.8)$$
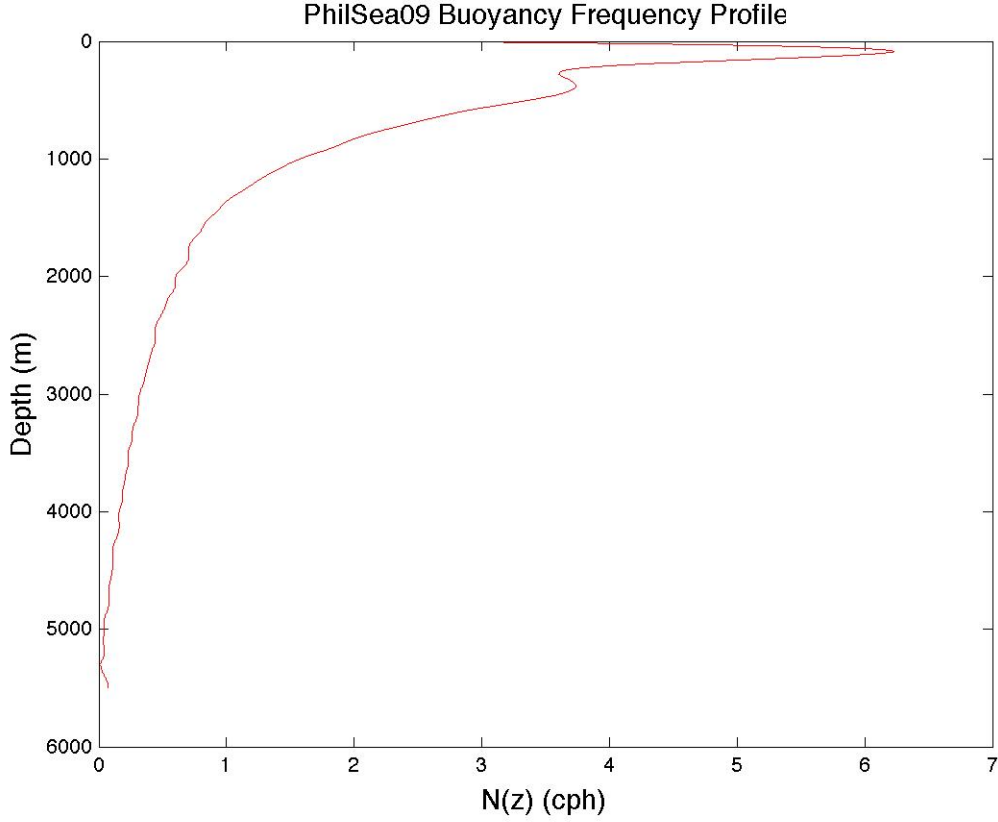
Figure 7.   NPAL pilot study buoyancy frequency profile (After Colosi et al. *2012)*.

The modal solution in Equation 2.9 is significant because it has within it, the components of vertical (standing wave) and horizontal (travelling wave) motion. The vertical motion is governed by the mode functions, $\psi_j(z)$ and the horizontal motion is governed by the propagation term, $e^{(i(kx+ly-\omega t))}$. Combined, they describe wave motion as vertical displacement over time, $\xi(r,t)$ and the nature of internal tide vertical scales.

$$\xi(r,t) \propto \psi_j(z)e^{(i(kx+ly-\omega t))}$$
(2.9)

Two examples of the solution to the linear internal wave mode equation (Equation 2.10), Modes 1 and 10, at the diurnal and semidiurnal frequencies are shown in Figure 8. In Equation 2.10, the horizontal wavenumber eigenvalue k_j is

13

equal to $\sqrt{(k^2 + l^2)}$. The diurnal and semidiurnal tidal constituents (frequencies) are represented by ω in Equations 2.9 and 2.10. The diurnal frequencies correspond with roughly one high and low tide per day whereas the semidiurnal frequencies correspond to two highs and lows. It can be seen from Figure 8 that there is frequency dependence with respect to the wave modes.

$$\frac{d^2\psi_j}{dz^2} + k_j^2\left(\frac{N^2 - \omega^2}{\omega^2 - f^2}\right)\psi_j = 0 \tag{2.10}$$
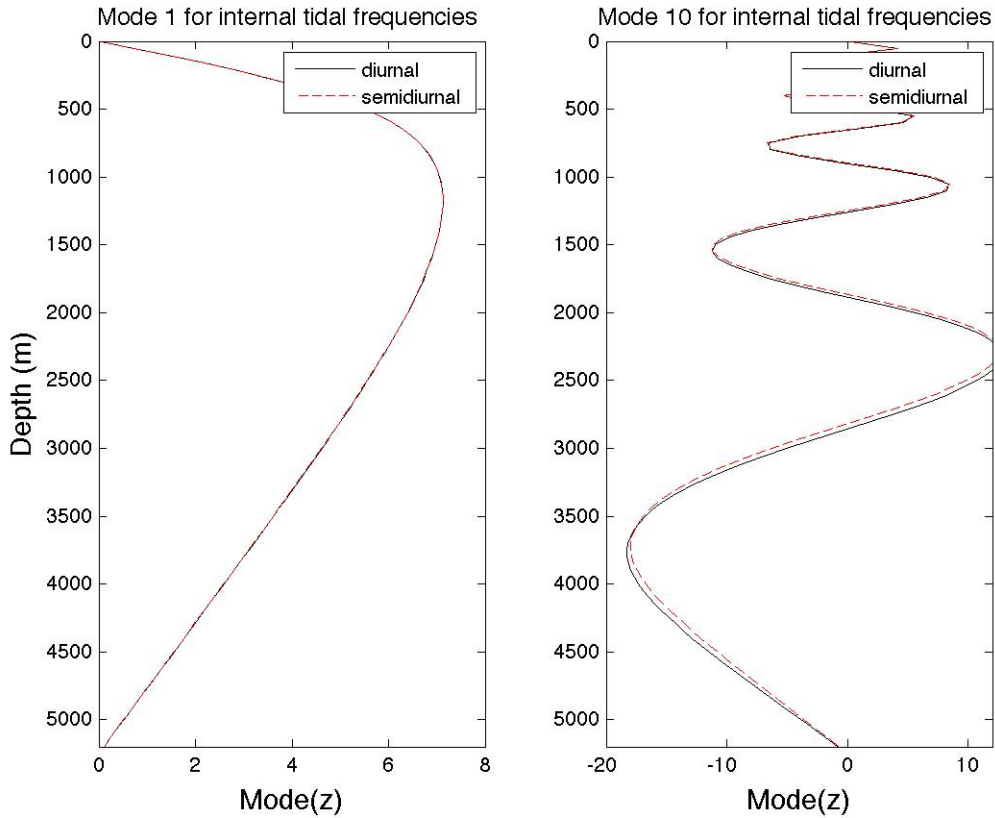
Figure 8. Internal wave modes 1 and 10 for diurnal and semidiurnal frequencies. This shows mode shapes have a dependence on frequency. Though, when comparing semidiurnal and diurnal frequencies, the difference is minimal.

By solving the wave equation, we can use the wavenumbers to get the horizontal wavelength (Table 1). The wavelengths λ in Table 1 are broken down

by mode number and tidal constituent (O1, K1, P1, etc.). The wavelengths are related to wavenumber k by the following relation, $\lambda = \dfrac{2\pi}{k}$.

Wavelength (km)							
Diurnal Constituents				Semidiurnal Constituents			
O1	K1	P1	Q1	M2	S2	N2	K2
516	433	438	576	167	161	171	160
246	206	209	274	79	76	81	76
49	41	42	55	16	15	16	15
24	20	21	27	8	8	8	8
10	8	8	11	3	3	3	3

Mode # : 1, 2, 10, 20, 50

Table 1.   Wavelengths for diurnal and semidiurnal constituents, and their respective mode number.

As can be seen from Table 1, the mode one horizontal wavelength of the principle lunar semidiurnal tidal constituent (M2) is around 170km. This is comparable with previous work done by Kerry et al. (2013). Preliminary analysis conducted in this section and the theory involved was critical to the analysis of internal tide energy (Section II-C) and in generating a regional model (Section II-E).

B.   DIURNAL AND SEMI-DIURNAL

The tracked isopycnals and isotherms at each mooring served as an accurate representation of displacement. The displacement time series used in this thesis were previously filtered by Colosi et al. (2012) to remove frequencies greater than 500 cpd. To verify the strong diurnal and semidiurnal signals present at both DVLA and T1 during the monthlong experiment, a spectral analysis was conducted on the tracked isopycnals for several depths at both locations.

At each depth, the mean displacement was subtracted from the data to find the displacement amplitude about the mean. A Hanning window was applied to compensate for leakage due to the time series not being periodic and to filter

out some of the ultra low frequencies. The data were converted from the time to the frequency domain by taking the discrete Fourier transform. Sampling frequency was 1/60 seconds.

To find the peak frequencies, the amplitude spectra were averaged across depth. Results showed that below the surface layer, the internal wave structure between DVLA and T1 is dominated by waves traveling at the diurnal and semidiurnal frequencies (Figure 9). Since we were concerned with quantifying the effects of internal tides on acoustic variability, only the diurnal and semidiurnal frequencies were isolated in further processing of the data.
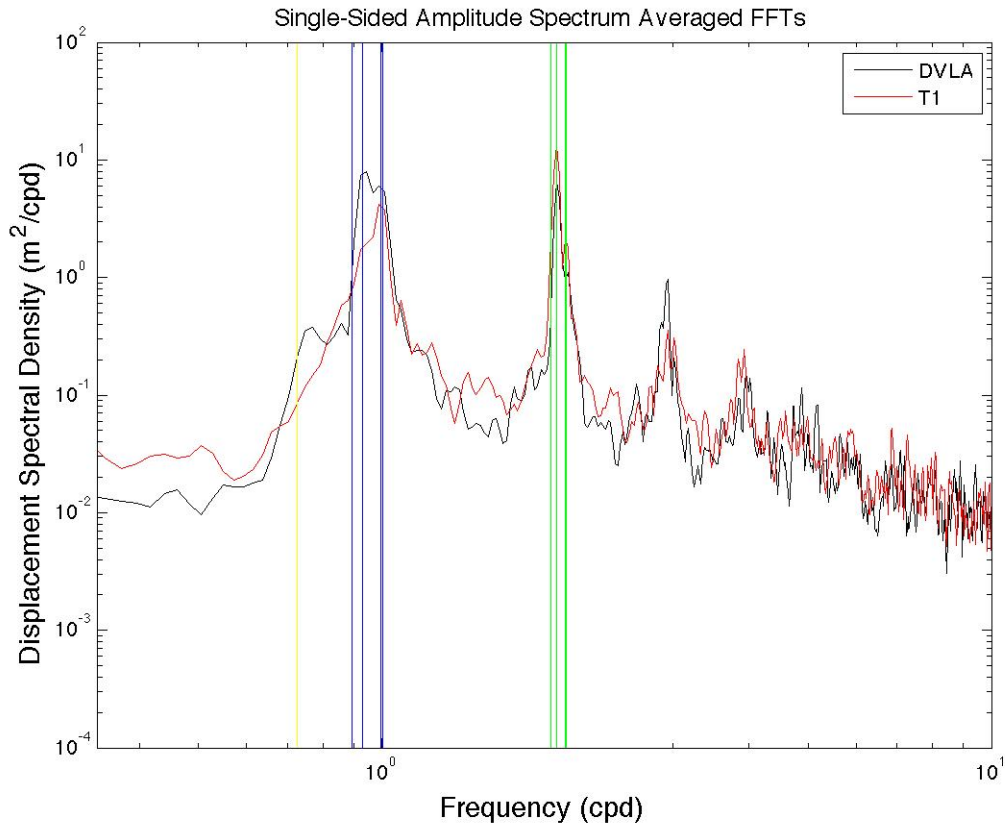
Figure 9.   Average of amplitude spectra across depth highlights peak amplitudes at diurnal and semidiurnal frequencies. The yellow vertical line corresponds to the intertial frequency. The blue vertical lines correspond with diurnal frequencies (O_1, K_1, P_1, Q_1). The green vertical lines correspond to semidiurnal frequencies (M_2, S_2, N_2, K_2).

At DVLA, the diurnal frequencies dominate but at T1, the semidiurnal frequencies dominate (Figure 9). This is not an unexpected result due to the complex bathymetry at the tidal generation zone contributing to spatial interference (Colosi et al 2012). Upon determining that the diurnal and semidiurnal frequency bands were the most dominant in the internal wave structure, a least-squares fit in time was applied to the displacement data (Figure 10). A weighted least-squares method (Equations 2.11-2.12) was used in fitting the unfiltered data to 8 diurnal frequencies ($O_1,K_1,P_1,Q_1,J_1,NO_1,ALP_1,OO_1$) and 7 semidiurnal frequencies ($M_2,S_2,N_2,K_2,L_2,MU_2,\lambda_2$) (Stewart 2013).

$$P=[E^T R^{-1}E]^{-1} \qquad (2.11)$$

$$A_{\omega}=PE^T R^{-1}A_{(\rho,°C)} \qquad (2.12)$$

From Equations 2.11 and 2.12, P is a matrix of tidal amplitude uncertainties, E is a matrix that contains the estimated internal tidal frequencies, R is the squared data error and $A_{(\rho,°C)}$ is a matrix of tracked internal wave amplitudes (isotherms and isopycnals). Weighted amplitudes A_{ω} from the least-squares fit were multiplied by the sine and cosine of the tidal frequencies in each of the 2 frequency bands. Then, the components for each frequency were summed up with respect to time in order to create the filtered wave spectrum for each frequency band. Time sampling in data processing was every 30 minutes. Two separate time series (diurnal and semidiurnal frequencies) were generated for each depth. Data error in performing the tidal fit was assumed to be .6m, as determined by Colosi et al (2012).
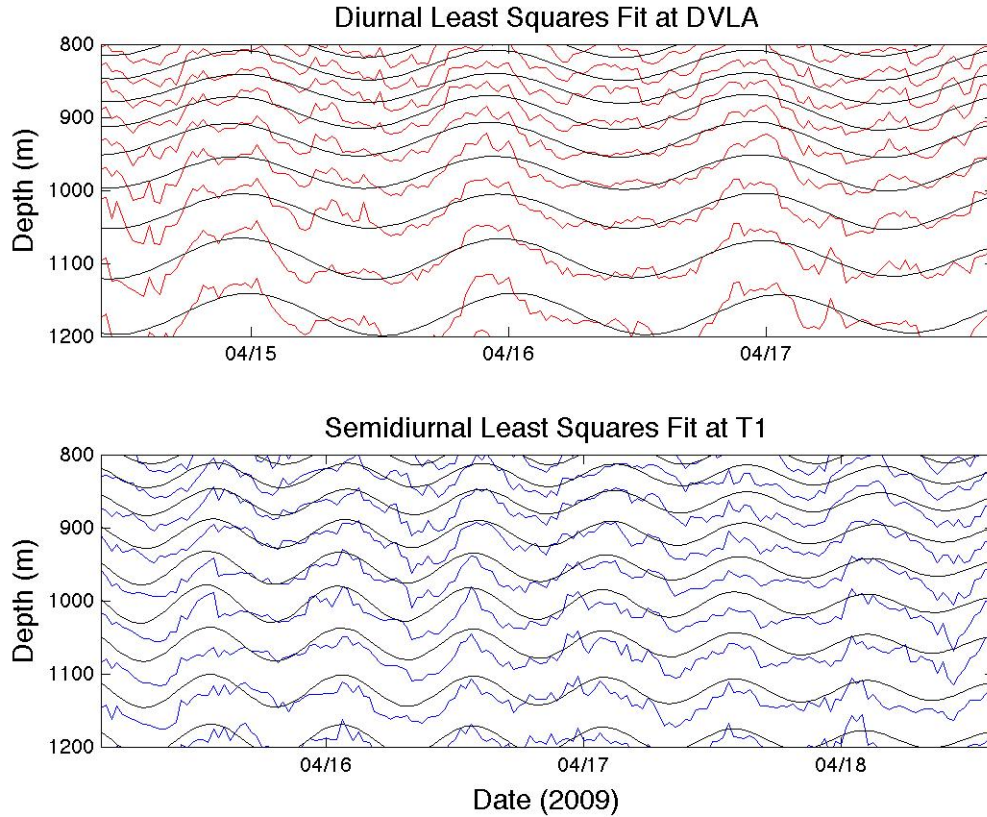
Figure 10. Least-squares fit to displacement for diurnal tidal components at DVLA and semidiurnal tidal frequencies at T1. Raw data is red and blue. Fit data is black.

C.   INTERNAL TIDE ENERGY

Internal tide displacement fluctuations are dependent upon depth, as can be shown by observing the RMS displacements for the tidal components at both moorings in Figure 11. It is apparent from Figure 11 that the RMS displacement does not follow a strict mode one shape across depth, inferring that the waveform is more complex than the mode one structure. Applying Equation 1.1 to the RMS displacements, we were able to get sound speed perturbations (Figure 12).

18
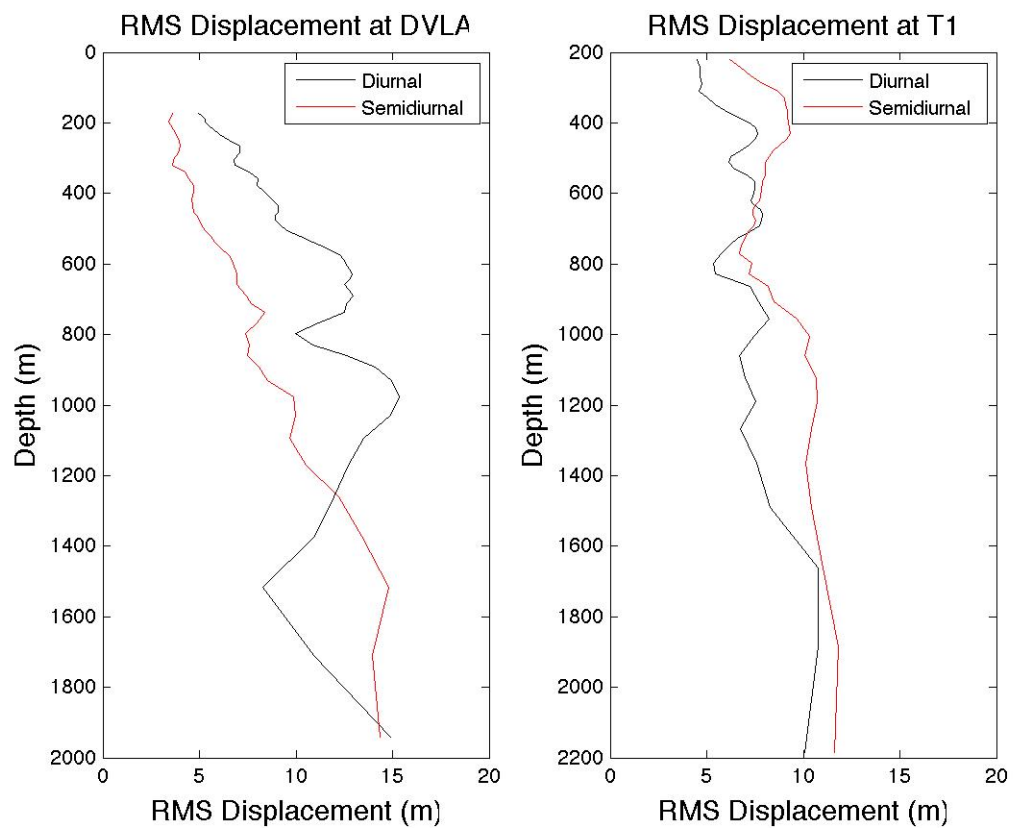
Figure 11. RMS displacements of tidal components at both moorings.
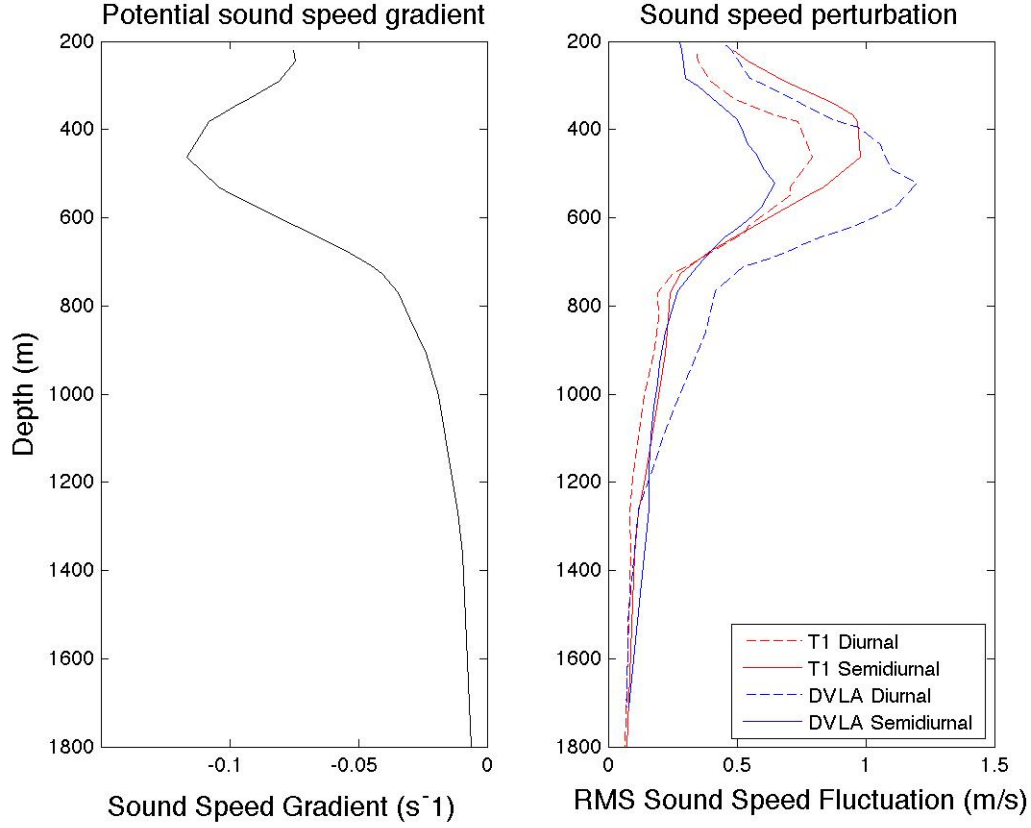
Figure 12. Potential sound speed gradient and sound speed perturbations for T1 and DVLA tidal components.

To determine the contribution of different modes to the structure of the waveform, we had to determine the energy contributions from these modes (Colosi et al. 2012). 50 modes were fit to the semidiurnal and diurnal displacement time series at both moorings using Equations 2.13 and 2.14, and the Gauss-Markov estimator (Equations 2.15-2.16) (Colosi et al. 2012). In Equations 2.13 and 2.14, $\xi(z,t)$ Is defined as the displacement from the mean for each depth over time, y is a matrix of observed covariances defined by $<\xi(z_1)\xi(z_2)>$, E is a matrix of mode shape products defined by $\phi_j(z_1)\phi_j(z_2)$, and n_y is noise associated with displacement estimates across depth.

$$\xi(z,t) = \sum_{j=1}^{J} a_j(t)\phi_j(z) + n_y \tag{2.13}$$

$$y = Ex + n_y \qquad\qquad (2.14)$$

In Equations 2.15 and 2.16, δx is defined as the difference in displacement in the x direction ($x - x_o$), δy is the difference in displacement in the y direction ($y - y_o$), S is the a-priori covariance of δx, R is the a-priori covariance of the noise, and P is the covariance of δx.

$$\delta x = (S^{-1} + E^T R^{-1} E)^{-1} E^T R^{-1} \delta y \qquad\qquad (2.15)$$

$$P = (S^{-1} + E^T R^{-1} E)^{-1} \qquad\qquad (2.16)$$

The mode energy distribution (Figure 13) was found by taking the RMS value of the mode amplitudes $a_j(t)$.
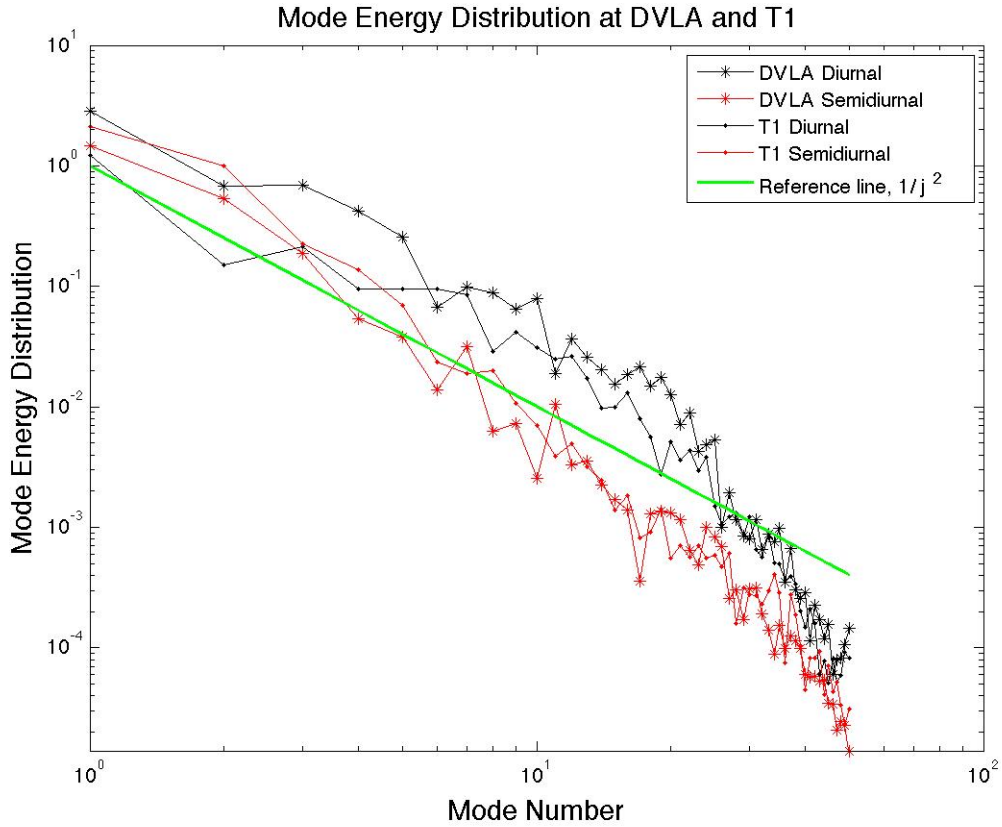
Figure 13. Energy (RMS($a_j(t)^2$))of 50 modes for tidal components at DVLA and T1 moorings.

Though the wave spectrum is more complex than the mode one structure, most of the energy distribution is present in mode one. However, there is noticeable energy associated with higher modes. There may be some acoustical variability associated with higher modes but we will be focusing on mode 1. Figure 13 shows that mode one in the tidal components of the waveform traveling from DVLA to T1 is the largest contributor of energy in the water column. Therefor, we would expect to see a significant amount of acoustic variability from the waveform to come from the mode one tidal components.

D.   INTERNAL TIDE SOURCE REGION

Two prominent and well-documented source regions for internal tide generation in the Philippine Sea are the Luzon strait in the South China Sea and the Sibutu Passage in the Sulu Sea (Girton et al. 2011). To develop a model for the region, utilizing the displacement data from DVLA and T1, a wave direction had to be assumed. Due to the experiments proximity to the Luzon strait, that location was assumed to be the source region with the propagation path heading due east, first passing through DVLA and then, T1. This is consistent with horizontal current observations during the NPAL pilot study. Taking into account the assumed path of propagation, the angle between DVLA and T1 was determined to be 72° relative to the propagation path (Figure 14).

Figure 14. Conceptualization of propagation path and angle between DVLA and T1. After https://maps.google.com/maps /ms?msid=213694482203726319071.0004e56fec1a8eab64184&msa =0&ll=21.371244,126.035156&spn=24.636776,27.070312.

E.   REGIONAL MODEL

To aid in future analysis and comparison with acoustic data obtained during the NPAL pilot study, a regional model was developed. The model was developed by combining weighted least-squares fits of the mode amplitude time series for the diurnal and semidiurnal frequency bands ($\alpha_n(\Omega)$ and $\beta_n(\Omega)$) at DVLA and T1 with the previously derived 50 mode shapes ($a_n(z)$) extrapolated across 5,500 meters, the depth of the water column. The wavenumbers (k) were multiplied by cos(72**°)** to project the wavenumber along the acoustic path. In order to get the combined diurnal/semidiurnal (Ω) amplitude components ($\xi(x,z,t)$) from the amplitudes of the two waves ($\zeta_{1,2}(x,t)$) across the 185 km range (x) between DVLA and T1 for each time step (t), the amplitudes

themselves needed to be weighted. The wave amplitudes (ζ_1 and ζ_2) were linearly weighted ($w_{1,2}(x)$) in the x-direction. At x=0km, the wave amplitude contributions from DVLA (ζ_1) were weighted (w_1) at 100%. At x=185 km, the wave amplitude contributions from T1 (ζ_2) were weighted (w_2) at 100%. 50% weighting was applied to each wave at the midpoint. Equations 2.17 and 2.18 were used to implement the model in Matlab.

$$\zeta_{1,2}(x,t) = \sum_{\Omega=f_1}^{f_2} \sum_{N=n_1}^{n_2} a_n(z)(\alpha_n(\Omega)\cos(kx-\Omega t) + \beta_n(\Omega)\sin(kx-\Omega t))$$

(2.17)

$$\xi(x,z,t) = \zeta_1(x,z,t)w_1(x) + \zeta_2(x,z,t)w_2(x)$$

(2.18)

Of note, the model is a data driven model that was developed for the Philippine Sea environment. Figures 15 and 16 were generated from the model. Figure 15 represents the sum of modes one and two of the tidal components and Figure 16 represents the sum of modes one through ten. The model has the ability to sum across all or a subsection of 50 modes and to separate the diurnal and semidiurnal components or to combine both parts in order to get the total internal tidal displacement between DVLA and T1.

Figure 15 shows the simplicity of the tidal amplitudes in the ocean between DVLA and T1 for mode one and two. Mode one accounts for the largest contribution of energy, of all the modes, in the water column. Figure 16 shows the complexity of accounting for more modes in the wave propagation between DVLA and T1. As more modes are taken into account, the wave structure becomes more complex and the total amount of energy accounted for in the water column increases, represented by an increase in the magnitude and spatial variability of tidal amplitudes. Analysis of multiple modes in comparison with acoustic data is significantly more complicated than comparison with mode one. Fortunately, mode one accounts for the majority of the energy in the water column and analysis of this mode was sufficient to accomplish the objectives of this thesis.
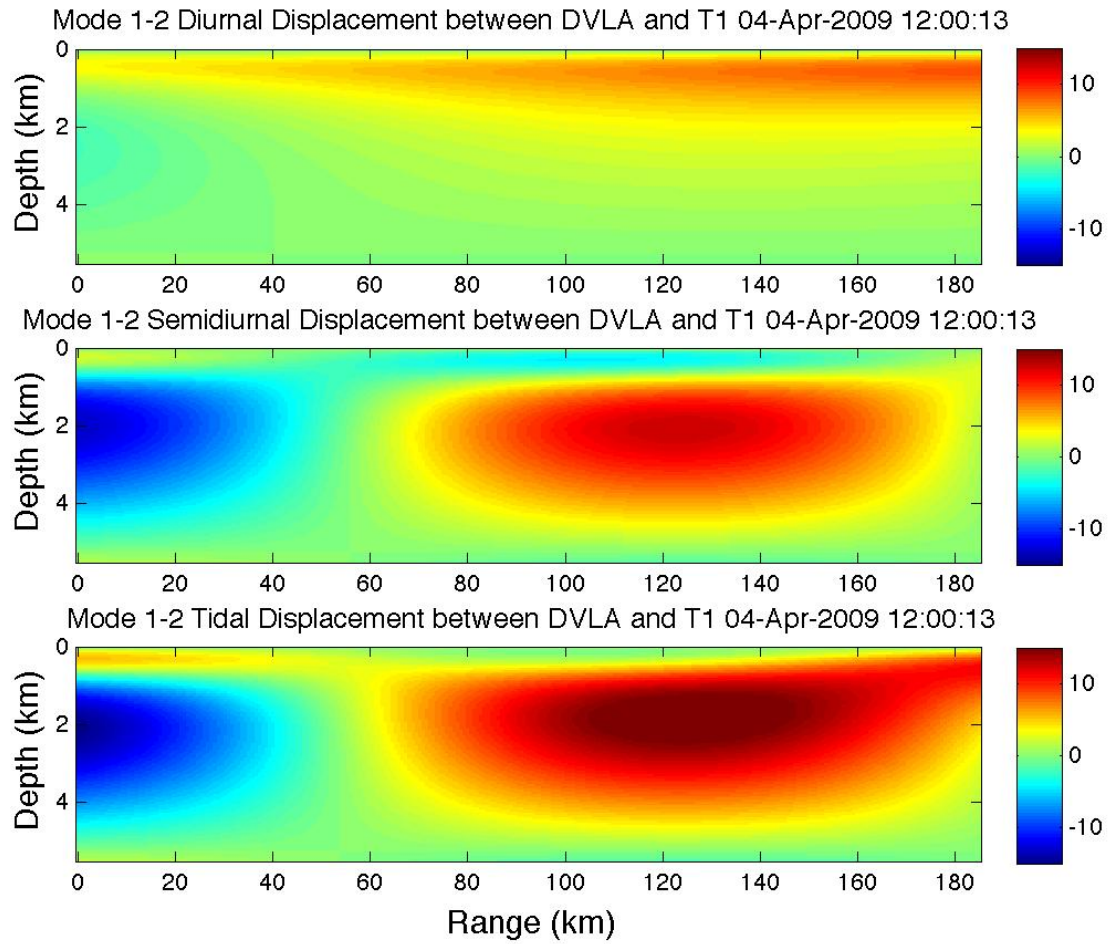
Figure 15. Internal tide model for the Philippine Sea, modes 1&2. Displacement is in meters.
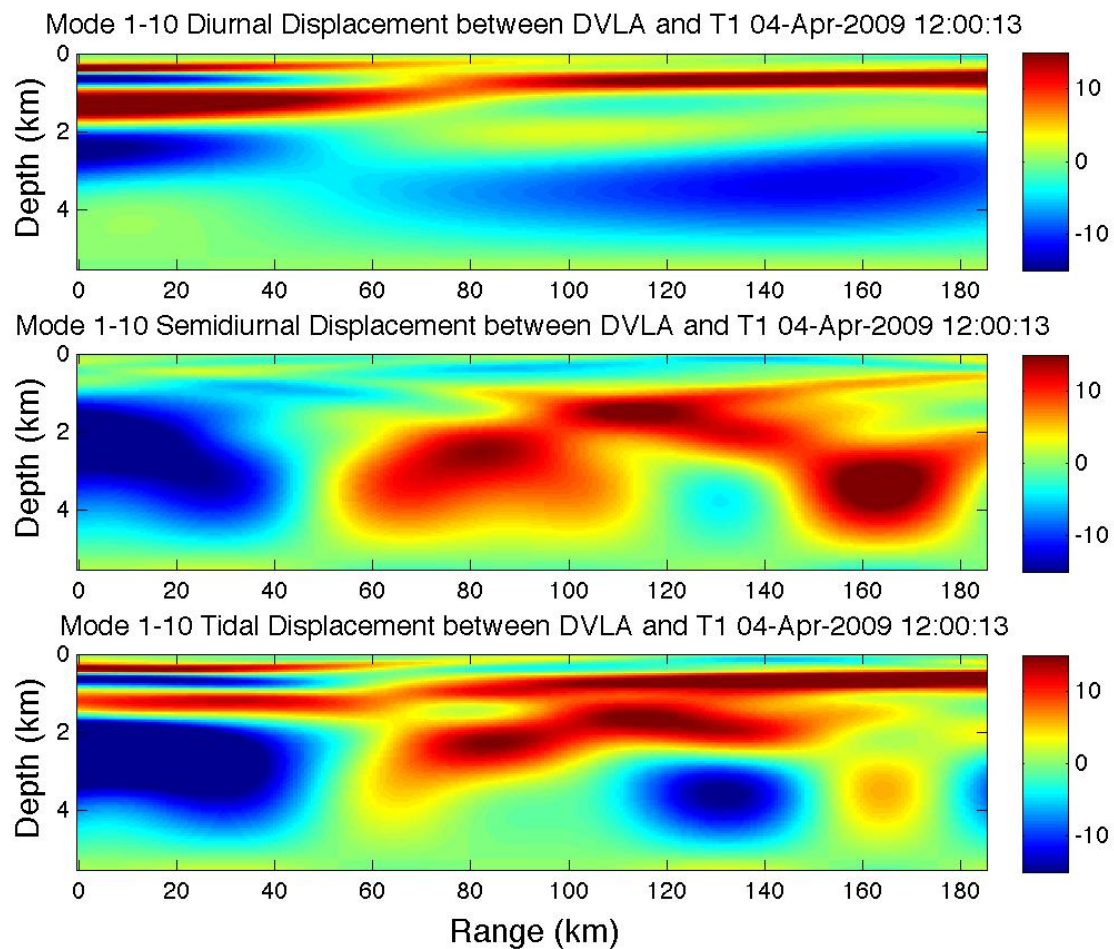
Figure 16. Internal tide model for the Philippine Sea, modes 1-10. Displacement is in meters.

III. ACOUSTIC ANALYSIS

Weston R.T. Coby conducted the acoustic analysis presented in this chapter.

The data collected during the NPAL pilot study were used for the examination of eigenray travel time, and intensity trends at multiple depths. A comparison of the eigenray travel time fluctuations with the internal tide displacements was used to determine if there was a correlation between the strength of the internal tides and travel time variation.

To conduct the acoustic analysis a prediction model was created for the eigenrays, and timefronts at four separate depths. The prediction model was then compared to the observed timefronts, and used to determine the ray path characteristics. Next, the Viterbi algorithm was used to track the eigenray timefronts. Finally, a statistical analysis of the actual acoustic data was conducted, to quantify the observed fluctuations.

A. RAY THEORY AND TIMEFRONTS

Ray theory is a high frequency approximation that describes propagation of sound rays through the ocean. In the deep water of the Philippine Sea, acoustic rays initially experience spherical spreading and later experience cylindrical spreading once they are vertically confined by the surface and bottom boundaries. As acoustic rays propagate away from a source, they are refracted, reflected, and scattered. This causes variations to their arrival angle, arrival time, and intensity of eigenrays at the receiver. Eigenrays are acoustic rays that travel from the transmitter and arrive at the exact location of the receiver. Ray theory makes the fundamental assumptions that there are no diffraction, that acoustic rays propagate as local plane waves, and that only small sound speed spatial changes take place over an acoustic wavelength.

Over the course of the pilot study eigenrays travelled from the T1 mooring source at 1,095m, to a receiver at a specific depth on the DVLA. The eigenray

properties are described through Equations 3.1-3.6. The ray speed is described by the group speed Equation (3.1), which states that acoustic wave energy follows the ray path at the group velocity, c_g. The group velocity is equal to the total derivative of the ray path ($d\bar{x}/dt$) with respect to time, and equal to the partial derivative of the plane dispersion relation, ω (Equation 3.2) with respect to the vector wavenumber, $\bar{k}$. The directional changes to the ray path are described by the refraction equation (Equation 3.3), which states that a changes to the vector wavenumber with respect to time are equal and opposite the changes to the dispersion relation (Colosi and Worcester 2013, unpublished manuscript).

$$d\bar{x}/dt = \delta\omega/\delta\bar{k} = \bar{c}_s \qquad (3.1)$$

$$\omega = \left(k_x^{\,2} + k_y^{\,2} + k_z^{\,2} \right)^{1/2} c(\bar{r}) \qquad (3.2)$$

$$d\bar{k}/dt = -\delta\omega/\delta\bar{x} \qquad (3.3)$$

The dispersion relation considers changes in a 3-D model (x, y, and z coordinates), yet the scope of this thesis only requires us to examine a 2-D ray slice containing the range and depth (x and z coordinates). The ray equations (Equations 3.4-3.6) use range as the independent variable (fixed transmitter and receiver) for a ray propagating in only the positive x-direction. From the CTD generated sound speed profiles we were able to get c(z), which we then used to solve the ray equations. The ray equations utilized data from both CTD profiles and buoys to predict the ray propagation paths from the dispersion relation, wavenumber (k_z), depth (z), and sound speed (c). The ray equations describe how the ray path changes as the ray travels from its source to the receiver. Because the ray equations are independent of the acoustic frequency, the ray paths will not change if the source frequency varies. Equation 3.4 calculates the ray's refraction describing the evolution of the ray's direction of propagation as it moves away from the source. Equation 3.5 calculates the ray's change in depth as it propagates. Equation 3.6 calculates the change in the ray's travel time as it propagates (Colosi and Worcester 2013, unpublished manuscript).

$$\frac{dk_z}{dx} = -\frac{\omega}{\left(c^{-2} - k_z^{\,2}/\omega^2\right)^{1/2}} \frac{1}{c^3} \frac{\partial c}{\partial z} \tag{3.4}$$

$$\frac{dz}{dx} = \frac{k_z}{\omega} \frac{1}{\left(c^{-2} - k_z^{\,2}/\omega^2\right)^{1/2}} = \tan\theta_r \tag{3.5}$$

$$\frac{dT}{dx} = \frac{1}{c^2\left(c^{-2} - k_z^{\,2}/\omega^2\right)^{1/2}} \tag{3.6}$$

This thesis focuses on sound rays propagating about the sound channel axis (depth at which the lowest sound speed occurs). The Ray Identification number (ID) describes the number of turning points within a ray. Acoustic waves with larger launch angles have lower IDs than acoustic waves with smaller launch angles. In deep water, lower IDs are more easily excited, meaning that these rays have more energy, and that there is a greater distribution of energy between launch angles. As sound rays propagate they are refracted toward regions with the slowest sound speed. This ray refraction is observed by the bending of the sound rays towards the sound channel axis as they propagate through the water column. The rays with the steepest launch angles and lowest IDs are expected to arrive at the receiver first, because they travel the farthest from the sound channel axis (SCA) and experience higher sound speeds. However, rays with shallow launch angles and large IDs are expected to propagate closer to the SCA, experience the slowest sound speeds, and arrive last.

The timefront plot (Figure 17) shows the pattern of a wavefront sweeping by a vertical set of receivers at a fixed range. Each wavefront branch is seen as the line between caustics (acoustic focusing points where the ray folds), and is composed of eigenrays with the same ID. The caustics farthest to the left of the timefront plot represent the rays with large launch angles and the fastest travel

times, while the caustics towards the right represent the rays with smaller launch angles and slower travel times.
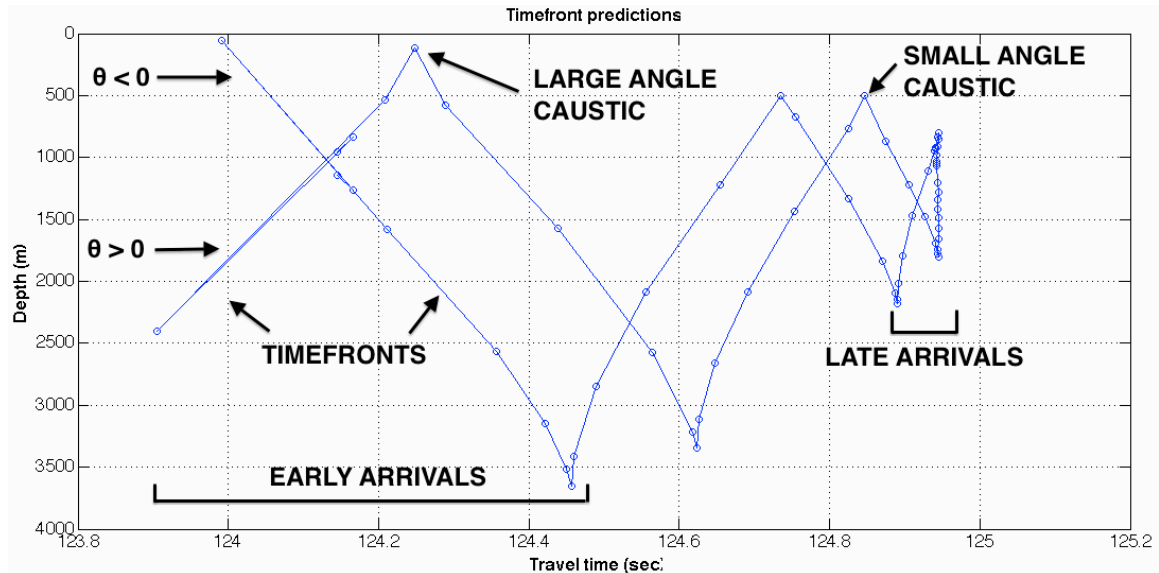
Figure 17. Plot of the predicted timefront.

The NPAL pilot study utilized a transmitter close to the sound channel axis to minimize acoustic interaction with boundaries, and to provide the greatest separation between the timefront branches (Figure 17).

The ray trace diagram shown in Figure 17 was used to determine the predicted Ray IDs, and turning depths. Rays that leave the source at positive angles with reference to the horizontal have positive ID values, while rays with an initial negative angle have negative ID values. A ray with a negative ID value will generally arrive ahead of a ray with the same positive ID value, and nearly equal launch angle.
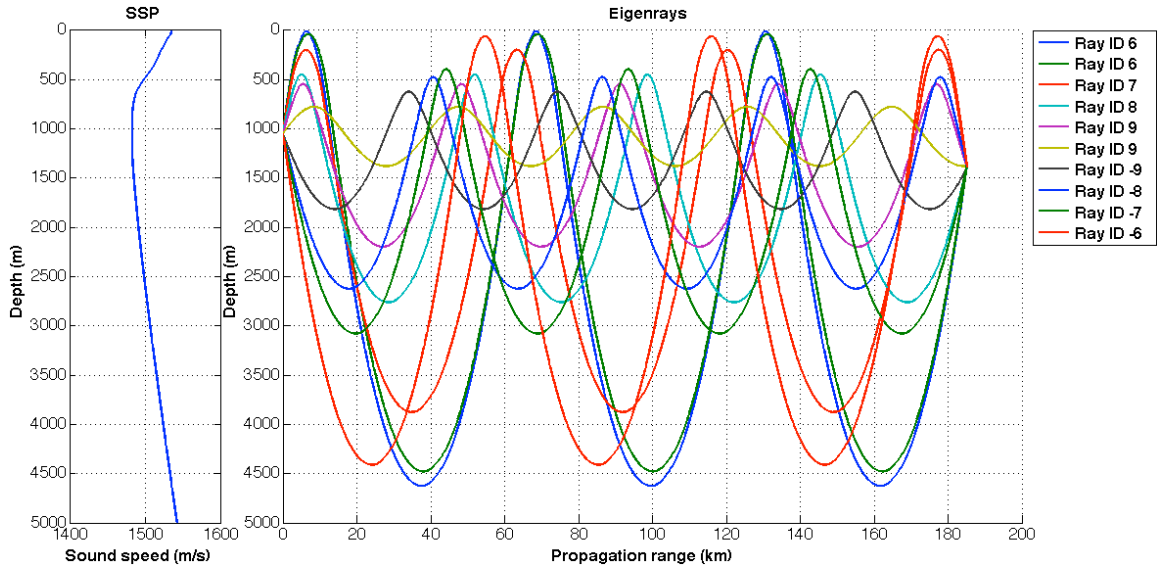
Figure 18. Plot of the predicted eigenrays for the 1,385m, receiver, derived from CTD sound speed profile. As the launch angle decreases the IDs increase.

The predicted Ray IDs correspond to the number of wavefronts seen in the timefront plot. The ray propagating closest to the sound channel axis (Ray ID +9) arrives last, while the ray with the steepest launch angle (Ray ID -6) arrives first.

B.   ACOUSTIC RAY TRAVEL TIMES

The pilot study consisted of 1,543 transmissions from the T1 mooring to the DVLA over a one-month period. The transmissions were sent out at intervals of 6 minutes and 3-hours. The acoustic data used for this thesis were collected from 24 receivers on the DVLA located at depths ranging from ~800 m to ~1385m. Four focus depths were chosen to provide insight on how the acoustic signals varied above the SCA (800m), along the SCA (1,000m), and between two receivers located within 100m of each other below the SCA (1,300m, and 1,385m).

An acoustic signal transmitted from a source (located at 1,095m) on the T1 mooring close to the SCA travelled to the DVLA mooring along several acoustic ray paths (Colosi et al. 2012). We used the ray equations to predict the

number of eigenrays, their paths, and timefronts for the four focus depths. Using inputs for the receiver depth, minimum and maximum launch angles, and launch angle step size we were able to create ray path predictions. Increasing the launch angle range, and decreasing the step size between launches, resulted in a noticeable increase in the number of predicted eigenrays. The optimum launch angle range was from -16° relative to the horizontal (SCA), to +16°, and the optimal launch angle step was .5°. Utilizing sub-optimal values decreasing the launch angle range, or increasing the step size resulted in fewer predicted eigenrays, excluding higher Ray IDs. Conversely increasing the launch angle range, or decreasing the step size made processing times unmanageably long.

The number of eigenrays predicted was dependent on the depth of the receiver relative to the transmitter. The receiver above the sound channel (800m) had eight eigenrays, none of which travel along the SCA. The number of eigenrays increased to thirteen at 1,000m (Figure 19) with several of those rays travelling along the SCA.
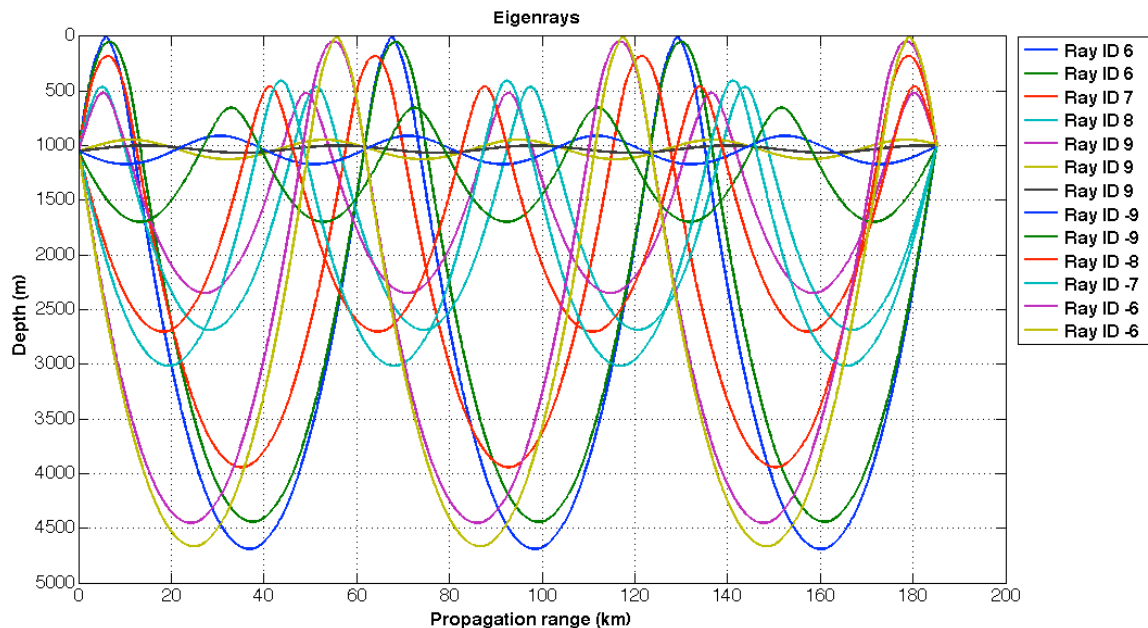
Figure 19. Predicted eigenray plot for 1,000m depth receiver. Improved eigenray resolution revealed additional eigenrays along sound channel axis.

Ten eigenrays were predicted at 1,300m and 1,385m (Figure 18), losing the larger numbered Ray IDs that were found at the 1,000m receiver depth. When the number of eigenrays increases, the ability to distinguish between each acoustic ray decreases due to the proximity of their arrivals. This congestion of arrival times is most pronounced near the SCA as the four slowest eigenrays arrive within .005 seconds of each other (Table 2).

Receiver Depth	1000m			
Ray ID	-9	9	9	-9
Arrival #	10	11	12	13
Launch Angle (Deg)	-4.75	0.25	0.75	-1.125
Turning Depth (m)	652.28	1000.23	946.91	910.90
End Time (s)	124.94	124.94	124.94	124.94

Table 2.　　1,000m Receiver Ray arrival times.

The acoustic data collected at DVLA were used to calculate SNR, which was then used to track the acoustic timefronts. The travel times for the tracked timefronts at the focus depths were then compared to the predicted arrival times to determine Ray IDs (Table 3).

Receiver Depth	800m												
Predicted ID	-6	-6		6	7	-7	-8	8	9				
Tracked Ray ID	-6	-6		6	7	-7		8	9				

Receiver Depth	1000m												
Predicted ID	-6	-6	6	6	7	-7	-8	8	9	-9	9	9	-9
Tracked Ray ID					7	-7							

Receiver Depth	1300m												
Predicted ID		-6	6	6	7	-7	8	-8	9	-9	9		
Tracked Ray ID		-6	6	6	7	-7	8						

Receiver Depth	1385m												
Predicted ID		-6	6	6	7	-7	8	-8	9	-9	9		
Tracked Ray ID		-6	6	6	7	-7	8						

Table 3.　　Predicted Ray IDs and tracked Ray IDs for focus depths.

C.   TIMEFRONT TRACKING

Figure 20 shows an overlay of the predicted timefronts for the receiver depths, and the observed timefronts for the first transmission. The timefront overlay plot clearly shows that for this transmission while the lower Ray IDs are not accurately predicted, the higher Ray ID timefronts closely conform to the predicted timefront. Figure 20 shows that the observed timefronts for Ray IDs $\pm 6 \rightarrow \pm 8$ are easily distinguishable and relatively well spaced for the focus depths, while the ± 9 timefronts are difficult to isolate. Furthermore, it shows that as depth changes the spacing between the wavefronts also varies causing some rays to move closer together and others to move farther apart.
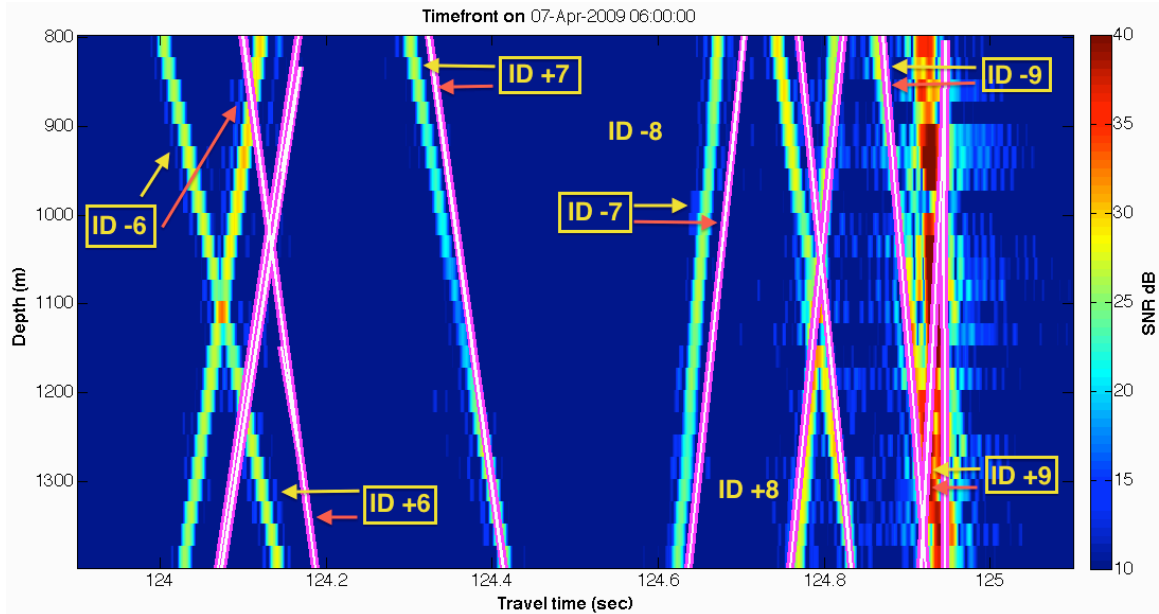
Figure 20. Observed transmission timefront with predicted timefront overlay.

Ray arrival plots (Figures 21-24) show the eigenray arrival times over the duration of the NPAL pilot study. The black dots in Figures 22-23 show the peak arrivals at the 1000m receiver depth with two different dB cutoffs (20dB and 25dB). Figure 24 shows the Viterbi tracked arrivals at 1,000m. Peak arrivals and the Viterbi tracking method will be discussed more in depth later in the section.

34

Figures 21 through 23 show that for the receiver at 1,000m the Ray IDs are harder to distinguish, and Figure 24 shows that only Ray IDs ±7 can be tracked. What cannot be seen from the timefront plots in Figures 21 through 23 is that Ray IDs ±6, and ±9 each have multiple eigenrays that cannot be readily distinguished.
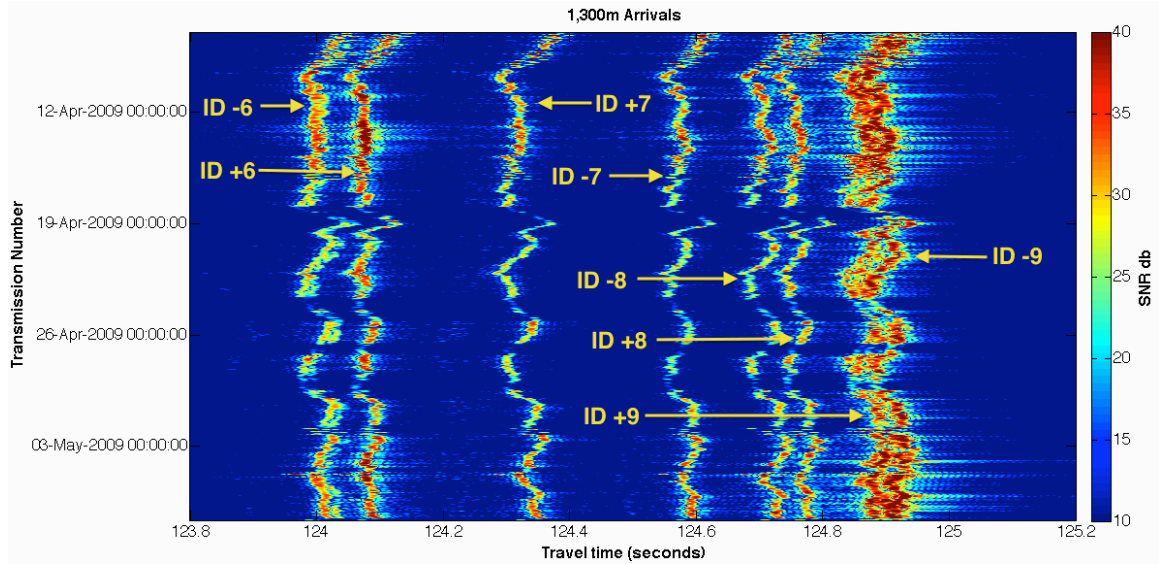
Figure 21. Time series plot of eigenray arrivals at 1,000m depth receiver.

The ray timefronts were tracked over the duration of the experiment in order to conduct a statistical analysis of the eigenrays. The Matlab *findpeaks* function was used on the SNR data to isolate receptions above a given threshold. Through trial and error it was found that a 20dB or 25dB threshold provided the best ray track at each depth (Figures 22 and 23), while a 30dB threshold left too many gaps in the arrival information, and a 15dB threshold did not eliminate enough noise. A 25db threshold limit was used in this thesis because it provided the cleanest eigenray tracks for further analysis.
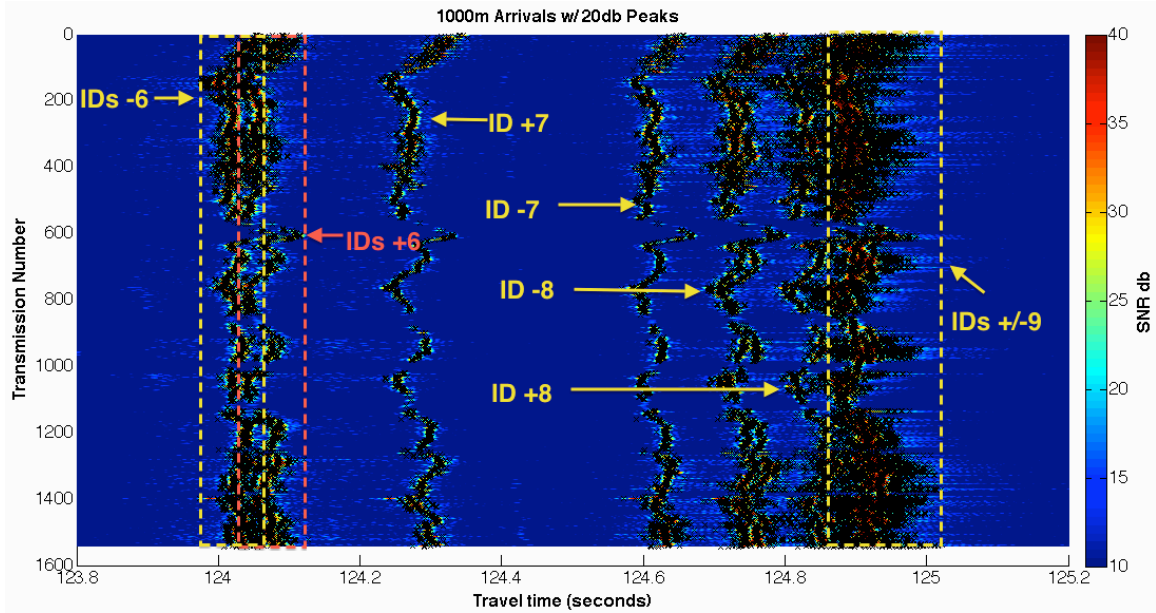
Figure 22. Time series plot of eigenray arrivals at 1,000m depth receiver with 20dB threshold SNR peaks
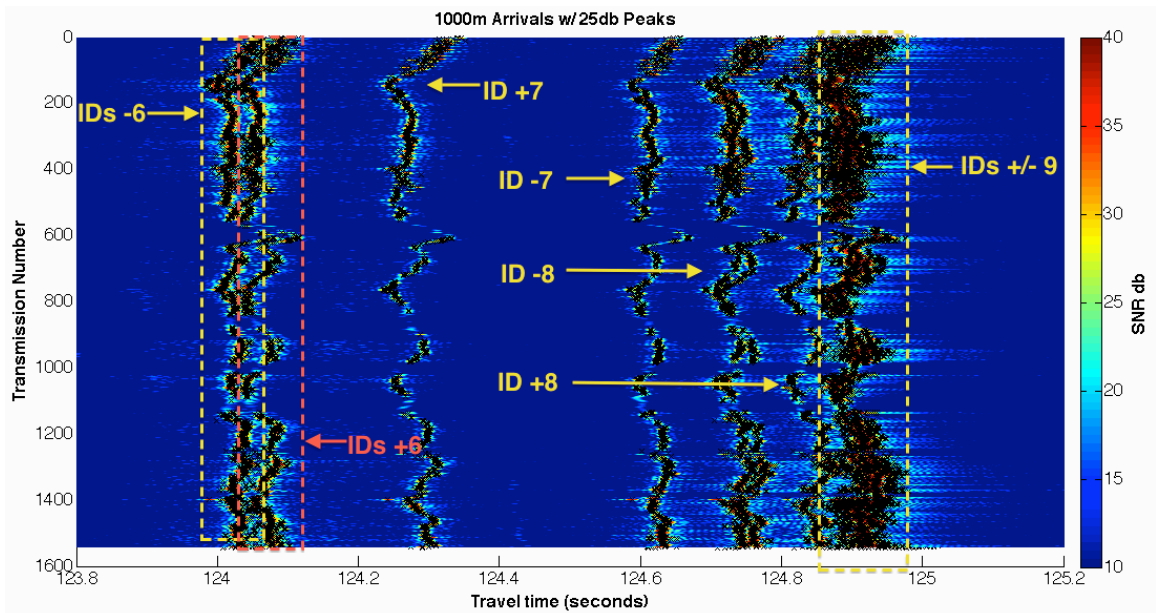
Figure 23. Time series plot of eigenray arrivals at 1,000m depth receiver with 25dB threshold SNR peaks

The Viterbi program is an automated tracking algorithm that was used on the 25db data to find the best track fit for each of the eigenrays (Dzieciuch and Worcester 2013, unpublished manuscript). The Viterbi program was designed to

track the timefront for a single acoustic ray. The Viterbi program accuracy was dependent on the ability to manually set the appropriate margins of error for each individual timefront. The program was capable of accurately tracking well-spaced timefronts with a high SNR, yet was not able to track closely spaced timefronts. The close proximity of the arrivals at the 1,000m receiver allowed only Ray IDs ±7 to be tracked by the Viterbi program (Figure 24). The Viterbi program works by creating a window, encompassing multiple peaks (Figure 23) for each sampling period, that is likely to contain the correct track. The Viterbi program then uses a Kalman filter to find the next most likely ray track position (Dzieciuch and Worcester 2013, unpublished manuscript), vice tracking only the highest SNR positions, or creating the straightest track from the first to the last reception. To find the most likely path, the Viterbi program utilized multiple physical parameter inputs, and limits, which required adjustments for each eigenray to create the most accurate track.
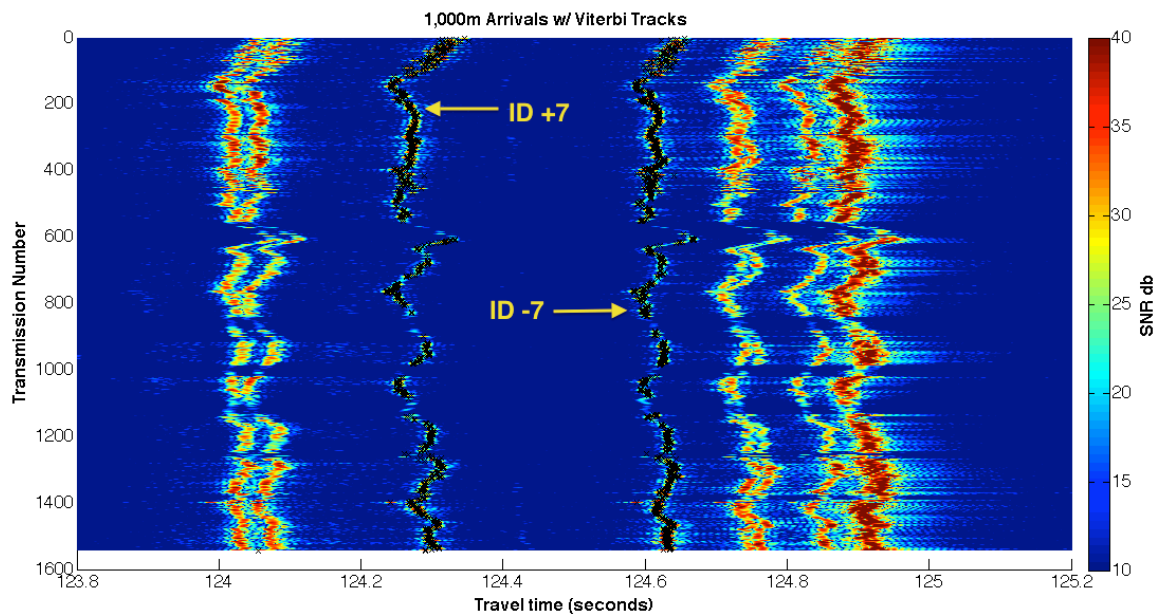

Figure 24. Time series plot of eigenray arrivals at 1,000m depth receiver with Viterbi track overlay

The ability to track each individual eigenray depended on correcting the allowable standard deviation (STD) for the next peak arrival time, and the STD next peak observation parameters in the Viterbi program. The less critical parameters used to fine-tune the eigenray track were the probability that the track continued/changed, and the probability of the track entering the designated gate (window). The windows needed to be sufficiently small to prevent the target eigenray's track from crossing over with the adjacent ray tracks. Decreasing the window size too much was problematic, as the ray tracks experienced large changes to the eigenray arrival times over a short period of time. These fluctuations resulted in the Viterbi program either losing the eigenray track, or crossing over between tracks. As noted earlier, the ray predictions for 1,000m, 1,300m, and 1,385m contain more than eight eigenrays. However, due to insufficient spacing between the highest Ray IDs of the 1,300m, and 1,385m eigenrays, the Viterbi program was only able to track the first six eigenrays. Similarly, due to the proximity of the adjacent eigenrays at 1,000m, only the middle two eigenrays could be tracked using the Viterbi algorithm.

The fluctuations in the ray time series (Figure 24) can be quantified by the travel time variation (Equation 3.7) and scintillation. The change in travel time (δt) due to sound speed fluctuations (δc) over the ray path (s) is shown in equation 3.7. The effect on intensity due to sound speed fluctuations is much more complicated and cannot be easily explained.

$$\delta t = \int \frac{\delta c}{c^2} ds \qquad (3.7)$$

D.   ACOUSTIC TIMEFRONT VARIABILITY

The ability and inability to track eigenrays over the duration of the NPAL pilot study led to the discovery of certain significant features. The eigenray arrival times varied significantly over the duration of the experiment, yet similar trends were observed for the tracked rays across the focus depths.

Over certain reception intervals the focus depths experienced similar drastic changes to the arrival times (Figure 25). The first 14 days of the experiment (07Apr 0000Z -21Apr 0300Z) are significant because of the highly variable SNR peaks, and eigenray arrivals, which made accurate tracking the individual eigenrays quite difficult. From 1145Z-1630Z on 30 April there was a significant increase in the eigenray travel times following a period of minimal (if any) SNR data, which prevented the Viterbi program from properly tracking the eigenray arrivals.
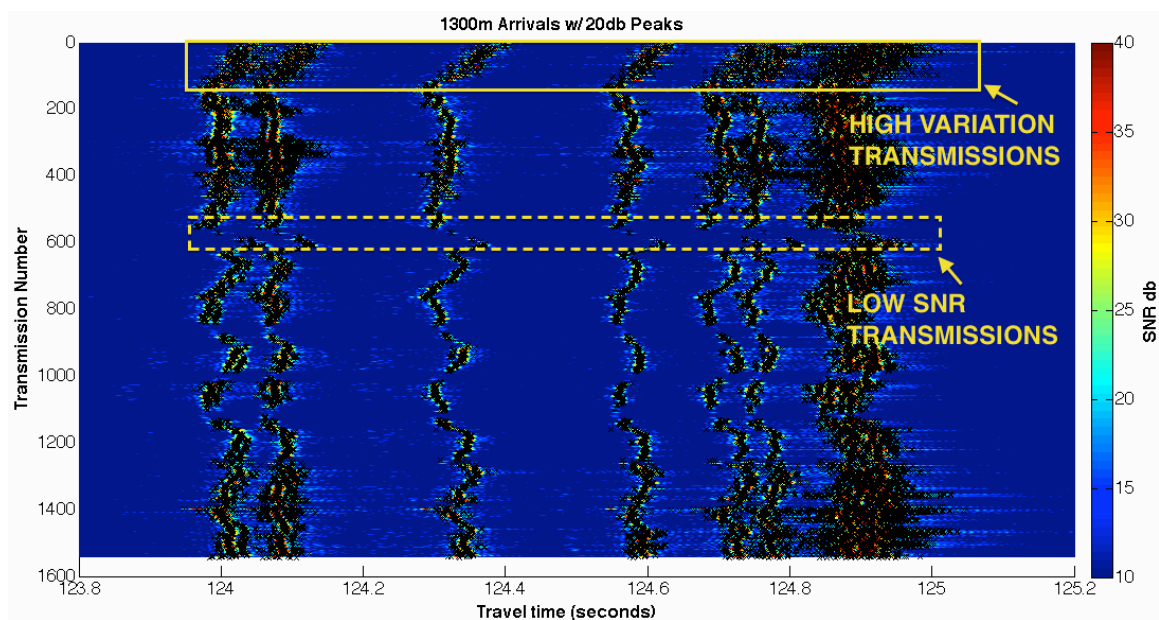
Figure 25. Observed SNR trends for time series plot of eigenray arrivals at 1,300m receiver depth (20db threshold)

At each of the focus depths Ray ID +9 had a significantly higher SNR value than the other rays. However, the Ray ID associated with the lowest SNR value varied with depth as shown in tables 4-7. The SNR values individual rays is significant because it shows that the the proximity of the eigenray paths is the determinate factor in whether or not the Viterbi algorithm can track the ray. Figure 26 shows the inability of the Viterbi program to track the Ray ID -8 arrival at the 800m receiver due to its initial proximity to Ray ID +8.
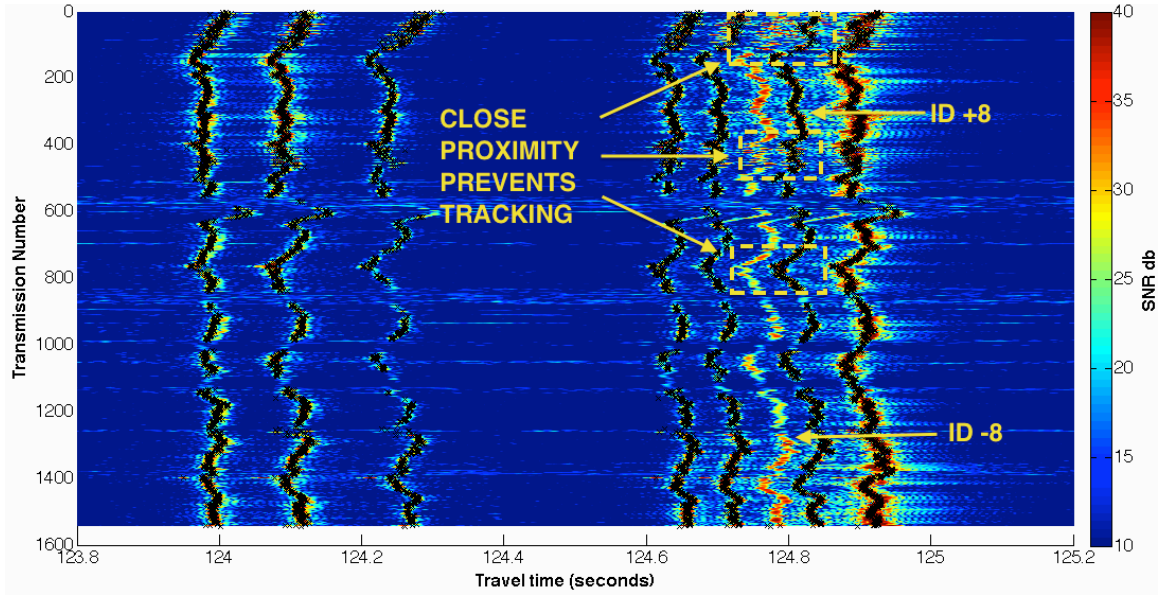
Figure 26.   Time series plot of eigenray arrivals at 800m depth receiver with Viterbi track overlay.

E.   TRAVEL TIME AND INTENSITY STATISTICS

A statistical analysis was conducted on each of the tracked timefronts to better understand how the ray timefronts varied throughout the experiment. The mean arrival time, arrival time variance, arrival time STD (wander), and the errors were calculated for each eigenray at the focus depths. Additional calculations were done to determine the peak broadband Intensity (I), Scintillation Index (SI) (Equation 3.8), intensity STD, and SI error. While the intensity calculations are too difficult to briefly explain, the SI is a measure of the intensity fluctuations.

$$SI = \frac{\langle I^2 \rangle}{\langle I \rangle^2} - 1 \qquad (3.8)$$

Tables 4-7 contain the data from the SI, and the statistical analysis for SNR and time. Tables 4-7 show that the eigenrays with the greatest launch angles arrive first yet have much lower SNR values than the eigenrays with the shallowest launch angles. The SNR variation for a fully saturated environment is approximately 5.6dB. From the tables it appears that only the rays propagating closest to the sound

40

channel axis experience SNR variation that is consistent with a saturated environment. As would be expected the scintillation index also appears to generally increase with decreasing launch angles. From the tables the phase variability appears to generally increase for all eigenrays as they approach the SCA and decrease as they move away from the sound channel axis.

Receiver Depth	800m						
Ray ID	-6	-6	6	7	-7	8	9
Arrival #	1	2	3	4	5	7	8
Launch Angle (Deg)	-14.72	-15.14	14.59	13.38	-10.25	9.03	8.09
Turning Depth (m)	42.51	0.02	58.43	171.36	412.13	468.96	508.73
Arrival Mean (s)	123.99	124.10	124.25	124.64	124.71	124.82	124.90
Arrival STD (s)	1.18E-02	1.65E-02	2.11E-02	1.82E-02	1.50E-02	1.84E-02	1.83E-02
Track Variance (s)	1.38E-04	2.71E-04	4.46E-04	3.31E-04	2.25E-04	3.37E-04	3.34E-04
SNR Mean (dB)	32.38	34.09	30.15	31.60	31.61	32.91	39.51
SNR STD (dB)	3.30	4.50	3.38	3.65	3.85	4.01	6.52
Scintillation Index	2.79	4.69	5.95	4.66	4.24	3.16	3.97
Phase Variability (rad/s)	20.31	28.44	36.48	31.44	25.91	31.74	31.59

Table 4.   800m Receiver tracked timefront statistics and SI. SNR statistics account for internal wave and mesoscale variability.

Receiver Depth	1000m	
Arrival #	3	4
Ray ID	7	-7
Launch Angle (Deg)	13.28	-10.38
Turning Depth (m)	180.85	405.73
Arrival Mean (s)	124.28	124.62
Arrival STD (s)	2.24E-02	1.80E-02
Track Variance (s)	5.00E-04	3.25E-04
SNR Mean (dB)	30.84	30.74
SNR STD (dB)	3.26	3.64
Scintillation Index	0.494	0.578
Phase Variability (rad/s)	38.65	31.13

Table 5.   1,000m Receiver tracked timefront statistics and SI. SNR statistics account for internal wave and mesoscale variability.

Receiver Depth	1300m					
Arrival #	3	1	2	4	5	6
Ray ID	-6	6	6	7	-7	8
Launch Angle (Deg)	-14.59	14.72	15.14	13.13	-10.55	9.41
Turning Depth (m)	58.43	42.51	0.02	194.90	396.68	452.30
Arrival Mean (s)	124.33	124.00	124.08	124.58	124.71	124.76
Arrival STD (s)	2.19E-02	1.54E-02	1.34E-02	1.72E-02	1.92E-02	1.67E-02
Track Variance (s)	4.78E-04	2.38E-04	1.78E-04	2.97E-04	3.67E-04	2.79E-04
SNR Mean (dB)	31.18	31.68	33.12	30.77	31.87	37.51
SNR STD (dB)	3.32	3.14	5.02	3.58	3.63	6.05
Scintillation Index	0.478	0.421	2.032	0.526	0.596	1.621
Phase Variability (rad/s)	37.78	26.65	23.07	29.78	33.11	28.85

Table 6.   1,300m Receiver tracked timefront statistics and SI. SNR statistics account for internal wave and mesoscale variability.

Receiver Depth	1385m					
Arrival #	3	1	2	4	5	6
Ray ID	-6	6	6	7	-7	8
Launch Angle (Deg)	-14.56	14.74	15.12	13.09	-10.59	9.47
Turning Depth (m)	61.06	39.99	0.00	198.64	394.16	449.47
Arrival Mean (s)	124.34	123.99	124.09	124.57	124.70	124.77
Arrival STD (s)	2.22E-02	1.49E-02	1.31E-02	1.70E-02	1.97E-02	1.62E-02
Track Variance (s)	4.93E-04	2.22E-04	1.72E-04	2.90E-04	3.90E-04	2.63E-04
SNR Mean (dB)	31.35	31.38	35.55	30.67	31.92	37.75
SNR STD (dB)	3.49	3.34	5.06	3.53	3.83	5.61
Scintillation Index	0.559	0.433	0.861	0.603	0.679	1.029
Phase Variability (rad/s)	38.38	25.77	22.67	29.43	34.11	28.00

Table 7.   1,385m Receiver tracked timefront statistics and SI. SNR statistics account for internal wave and mesoscale variability.

Figure 27 is a plot of the arrival wander for each of the eigenrays at the focus depths. The plot appears to show a general increase in arrival wander as the travel time increases.
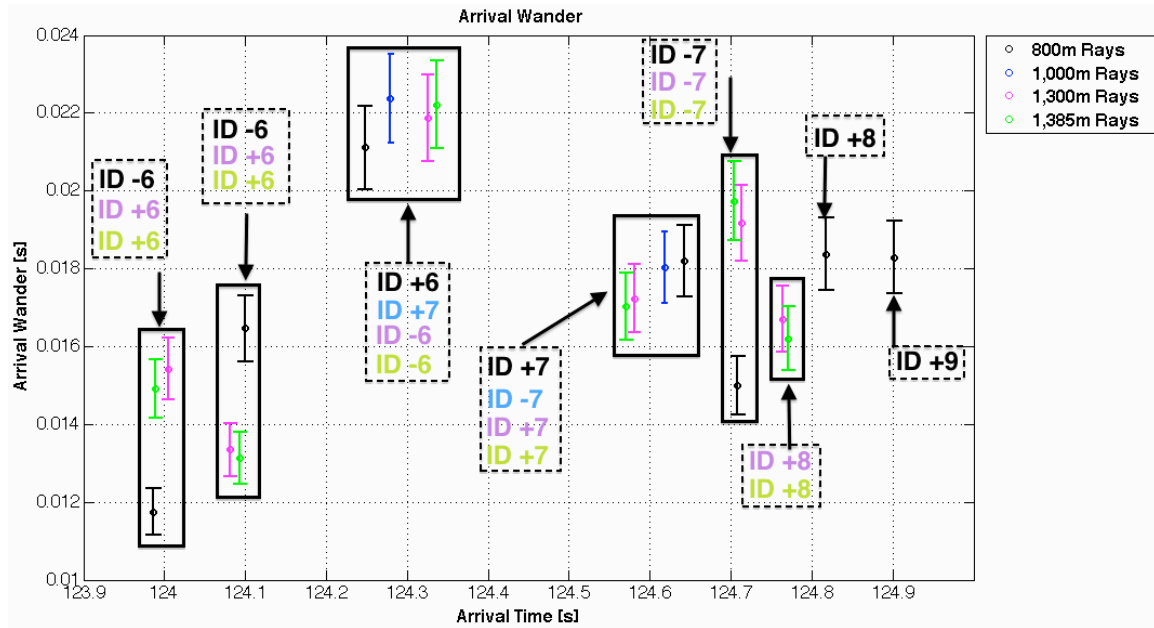
Figure 27. Plot of eigenray wander across the focus depths.

Figure 28 is a plot of the eigenray intensity variance across the focus depths. This plot shows that there is a general increase in the intensity variance as you increase travel time.
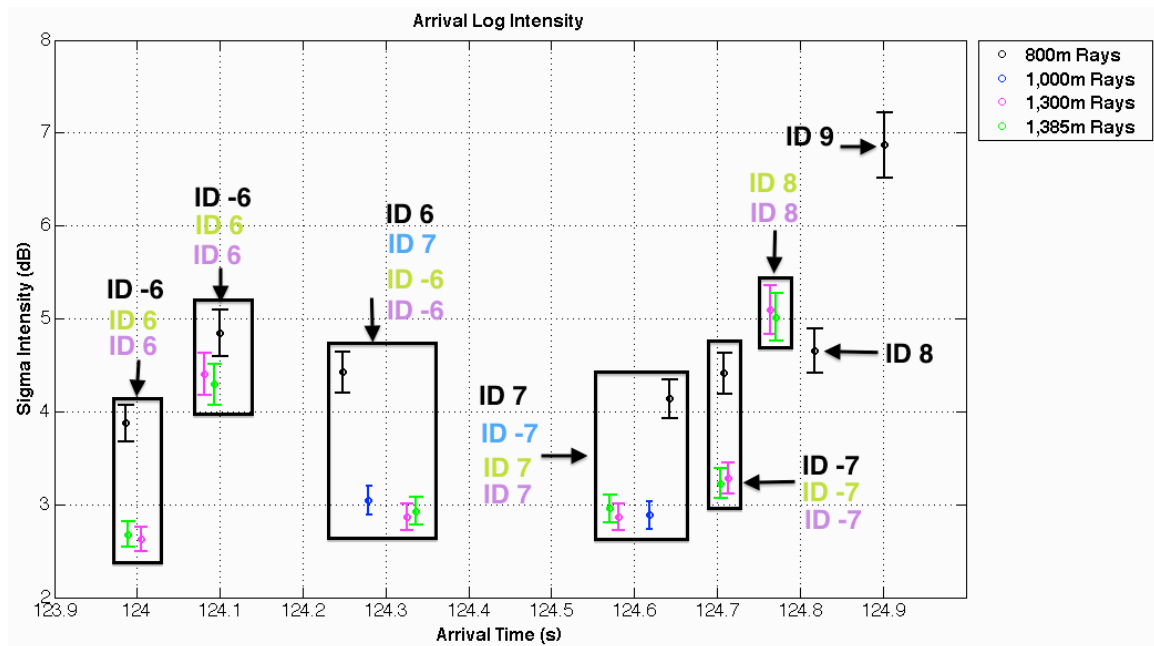

Figure 28. Plot of eigenray intensity variance across the focus depths.

THIS PAGE INTENTIONALLY LEFT BLANK

IV. OCEAN DATA AND ACOUSTIC DATA COMPARISON

Jacob A. Fischer, and Weston R.T. Coby jointly conducted the acoustic and oceanographic data comparison presented in this chapter.

A. TIDAL FIT TO ARRIVAL TIMES

Having determined that the internal tidal frequencies were the dominant frequencies, that mode 1 had the most energy within the internal wave traveling between DVLA and T1, and having successfully tracked individual rays through data analysis and using the Viterbi algorithm, the next step was to determine how much of the acoustic arrival time variability could be attributed to the internal tides. First, we needed to verify that there was a strong diurnal and semidiurnal signal in the acoustic arrival time fluctuations. This was accomplished by fitting the previously mentioned diurnal and semidiurnal frequencies to the Viterbi tracked ray arrival times by using the same weighted least-squares method discussed in Section II-B of this thesis. Data error in performing the tidal fit was assumed to be 5 milliseconds (1/sampling rate). As seen in Figure 29, there is a distinct diurnal and semidiurnal frequency pattern in the arrival time fluctuations for individual ray arrivals at each sensor depth.
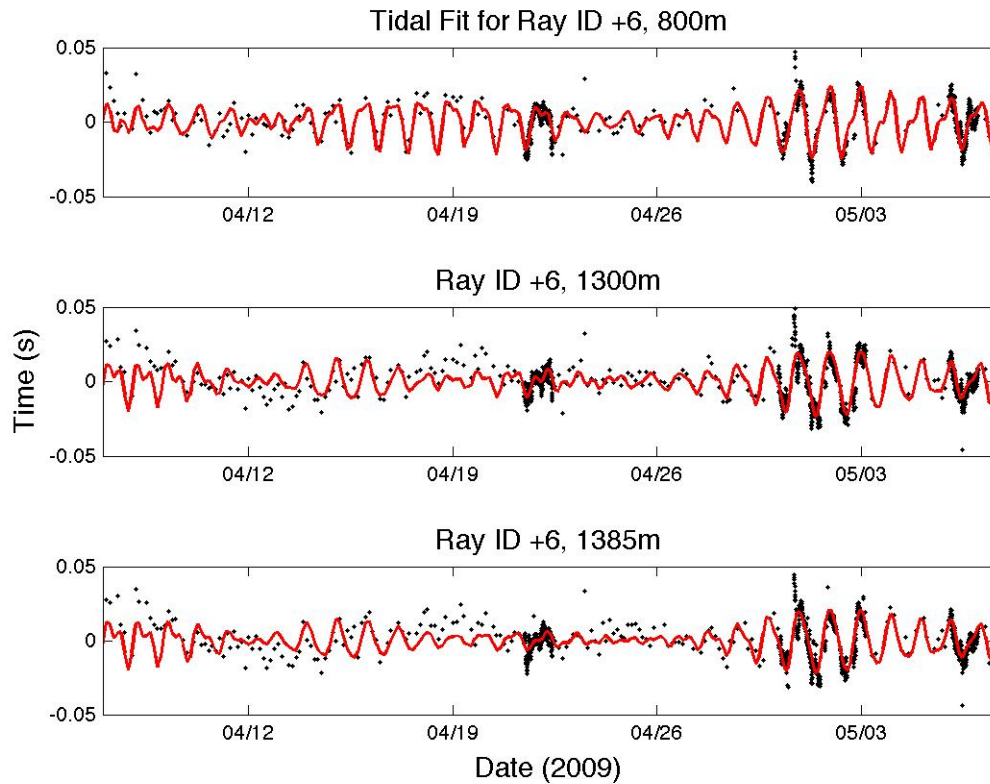
Figure 29. Internal tidal fit to the +6 Ray ID for sensor depth 800m, 1300m, and 1385m.

The sampling frequency changed during the monthlong study. Areas with a higher concentration of black dots in Figure 29, corresponds with times when the sampling frequency was 10/hour. Areas with a lesser concentration of black dots, corresponds with times when the sampling frequency was 8/day. There is a better fit during periods where the sampling frequency was 10/hour, as compared to other periods where the sampling frequency was 8/day, because there were more observations during those times. This brings up speculation that the fit may be unreliable in areas where sampling frequency was 8/day.

To evaluate the fit and determine the percentage of acoustic arrival time fluctuations that could be attributed to the tidal frequencies, a comparison of variability was conducted using Equation 4.1 for each of the tracked rays across the monthlong time period.

$$TF_\% = \frac{\sigma^2_{Fit(\omega,t)}}{\sigma^2_{Arr(t)}}$$
(4.1)

The percent acoustic arrival time fluctuation variability attributed to the internal tides ($TF_\%$) for the entire month is between 20% and 70%, depending on receiver depth and Ray ID (Figure 30).
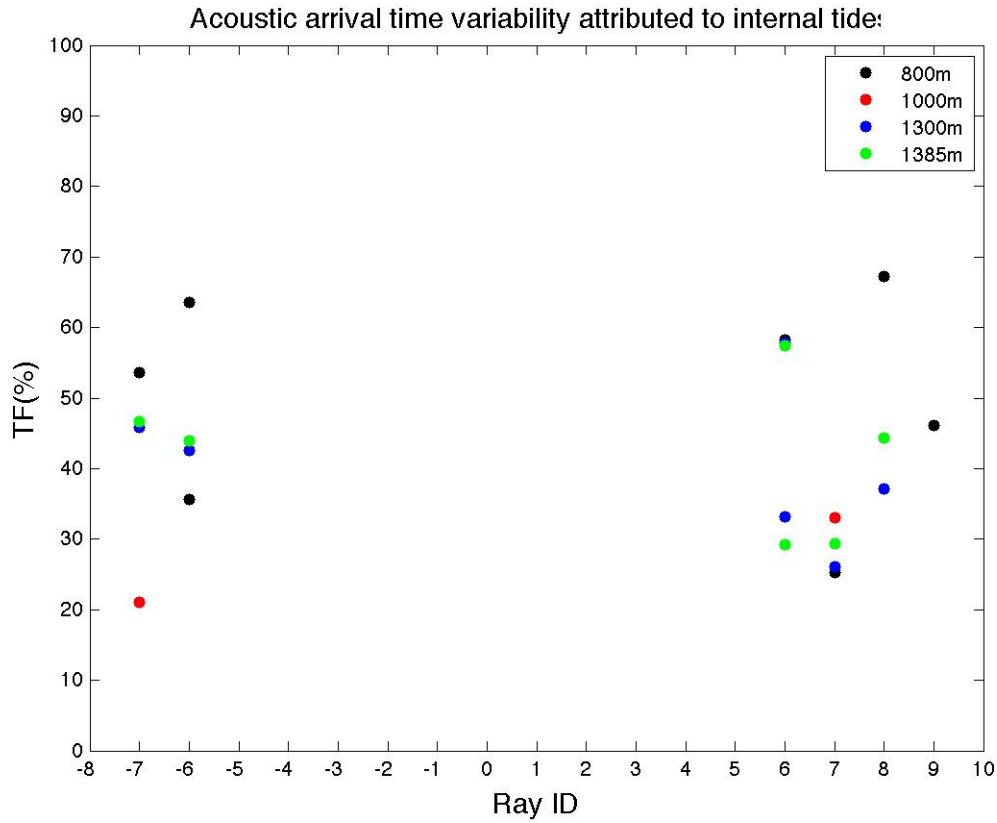
Figure 30. Acoustic arrival time variability attributed to internal tides for all tracked rays at each sensor depth.

To test the fit during periods of infrequent sampling, $TF_\%$ was calculated where sampling frequency was low, 8/day. We determined that the fit was slightly under predicting some of the arrivals by as much as 30% with a range of 0%-40%. Testing the fit during periods when the frequency sampling was high, 10/hour, $TF_\%$ was between 30-70%. These are expected results due to the least-

squares fit having more data/unit time during the higher frequency sampling periods. Taking the analysis one step further, we fit only the dominant diurnal (K_1) and dominant semidiurnal (M_2) frequencies. This showed a $TF_\%$ drop of 10%. This is an expected result due to the acoustic fluctuations being effected by multiple tidal frequencies; not just the two dominant frequencies.

For further comparison, the tidal fit of the acoustic arrival time fluctuations for Ray ID +6 at receiver depth 800m was overlaid on the mode 1 tidal fits of the oceanographic data for both DVLA and T1 (Figure 31). As was previously determined, there is a strong semidiurnal signal at T1 and a strong diurnal signal at DVLA. Two intriguing time windows to look at on this figure are between April 12-22 on the top panel and April 22-May 7 on the bottom panel. It is clear that the acoustic fluctuations match well to the mode 1 signal at DVLA between April 12-22 and to the mode 1 signal at T1 between April 22-May 7. From this, we could glean that the acoustic variability of Ray ID +6 at receiver depth 800m was affected more by the internal tidal signal near DVLA during the April 12-22 timeframe than by the signal near T1. However, during the April 22-May 7 timeframe, the mode 1 component of the internal tide near T1 had a greater impact on acoustic variability. Further analysis would be required to verify this hypothesis.
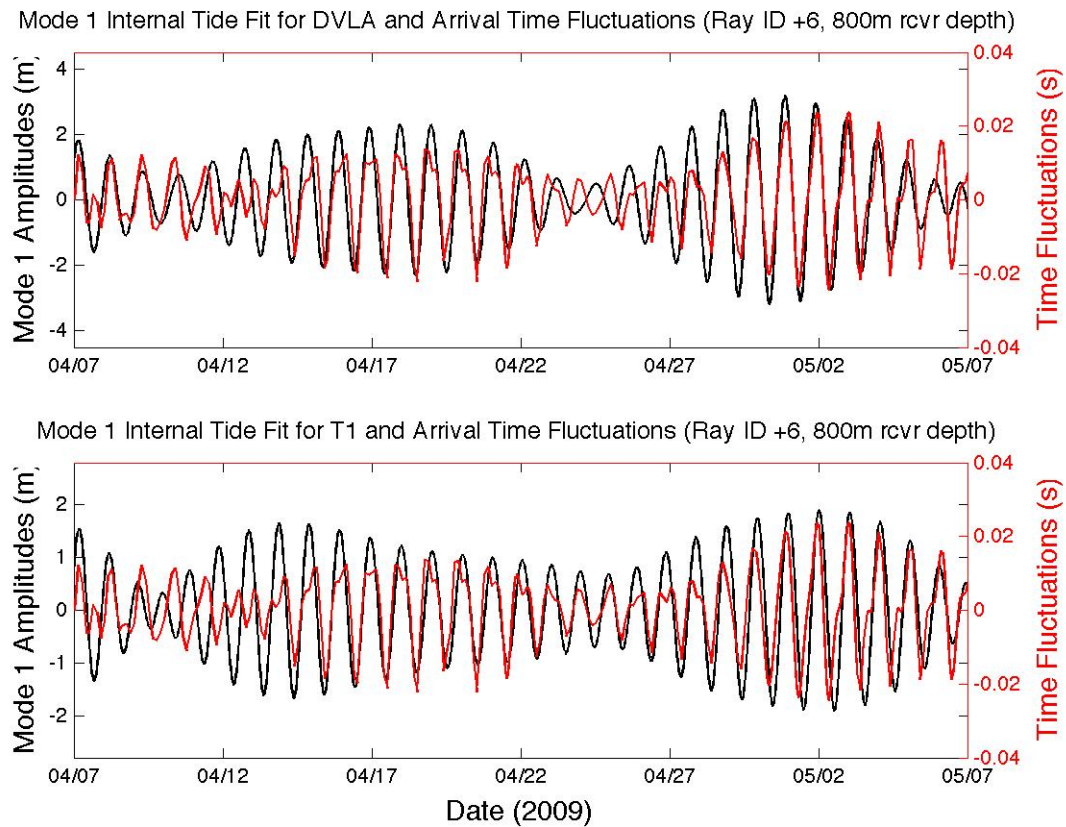
Figure 31. Tidal fit overlays for Oceanographic (black line) and Acoustic (red line) data sets. (Oceanographic data – Internal tide fit to Mode 1 amplitudes at DVLA and T1. Acoustic data – Internal tide fit to arrival time fluctuations)

B.   EFFECTS OF SPRING AND NEAP CYCLES

Upon determining that acoustic arrival time fluctuations were influenced by internal tides, the next step was to determine the times during the experiment when tidal amplitudes were strongest and weakest. This period of time is known as the tidal range, or more commonly, the spring/neap cycle. Tidal range is determined by the phase of the two dominant semidiurnal frequencies, M2 and S2. When M2 and S2 are in phase, you will have the strongest tidal amplitude and when out of phase, the weakest.

49

The spring and neap cycles were found by utilizing the previously fit internal tide displacement data. 50 mode amplitudes were fit to the data across time using the method described in Section II-C of this thesis. However, instead of fitting 15 frequencies to the mode amplitudes, only two frequencies, the M2 and S2 were fit. From the mode one time series, times corresponding to maximum and minimum amplitudes were identified. The inflection point between the maximum and minimum displacement amplitudes was used as the dividing time between spring and neap cycles. The spring/neap cycle where we had the most complete overlap of acoustic and oceanographic data, from 13 April, 2009 to 27 April, 2009, was chosen for analysis. Figures 32-33 show arrival time fluctuations overlaid on the mode displacement amplitudes. You can see from Figures 32-33 that there is some acoustic arrival time variability associated with the spring and neap cycles.
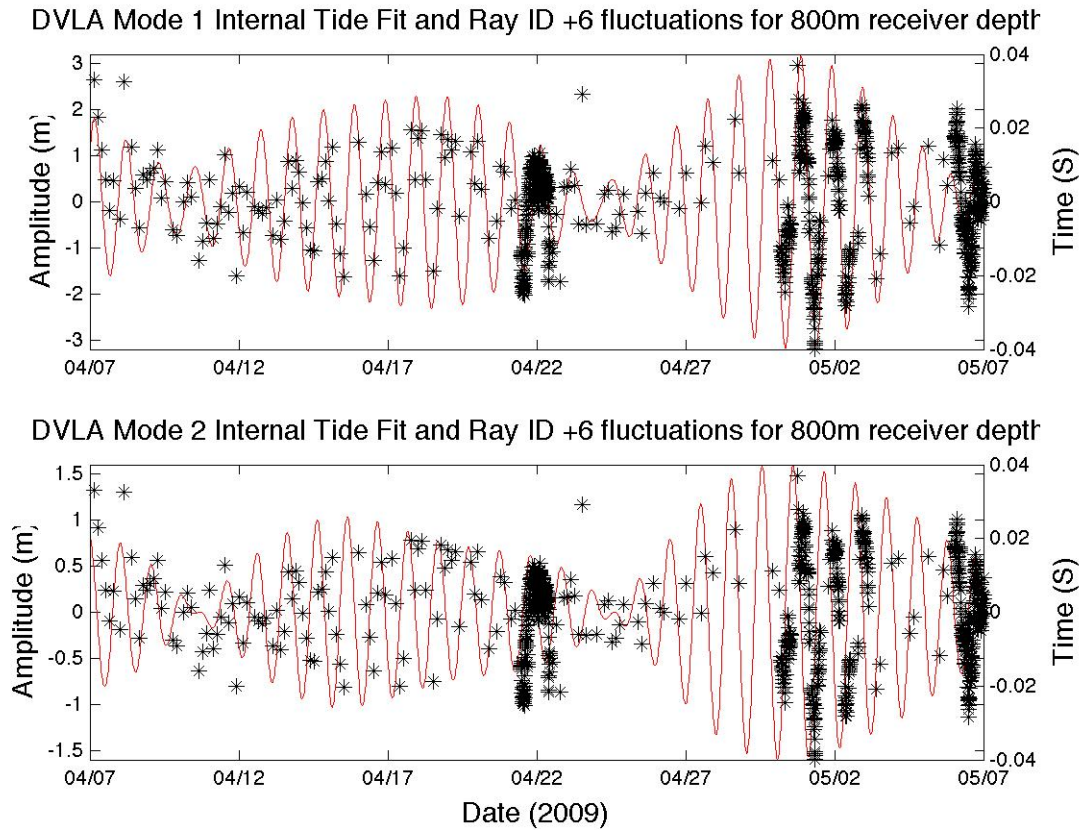
Figure 32. Mode 1 & 2 time series of amplitudes fit to the internal tides at DVLA shown with a red line. Arrival time fluctuations for Ray ID +6 at the 800m receiver depth are marked with black asterisks.
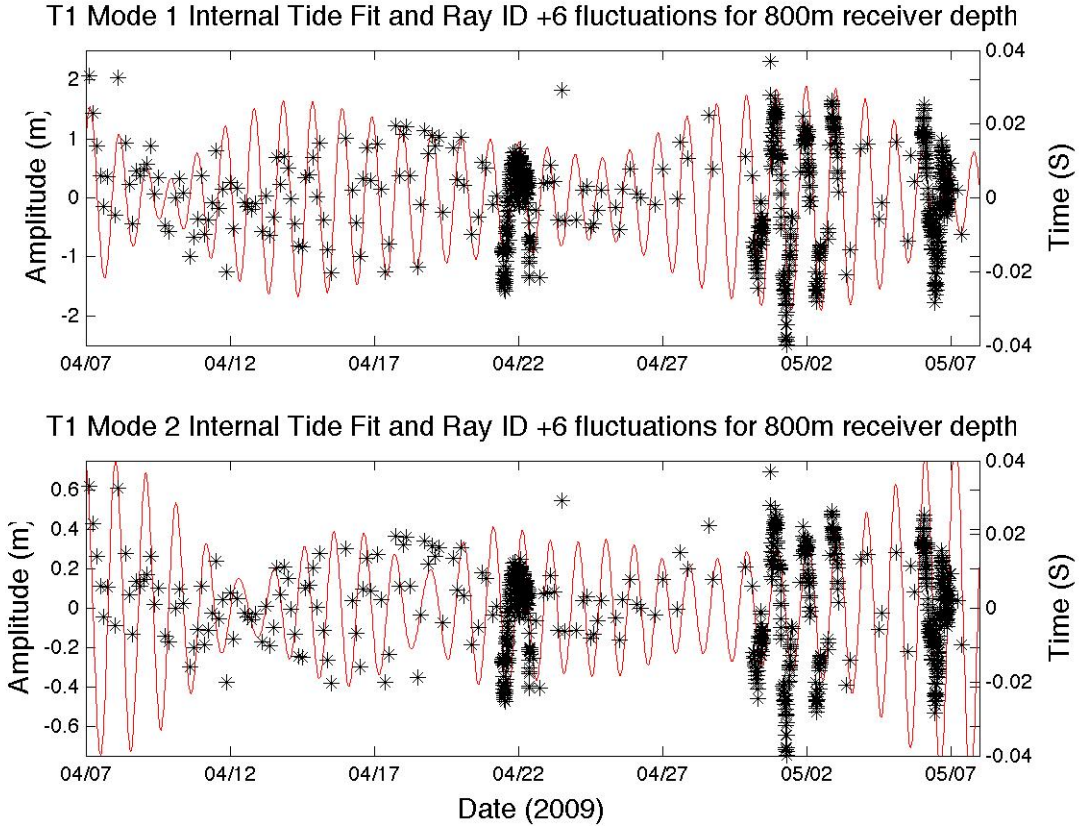
Figure 33. Mode 1 & 2 time series of amplitudes fit to the internal tides at T1 shown with a red line. Arrival time fluctuations for Ray ID +6 at the 800m receiver depth are marked with black asterisks.

It can be seen by looking at Figure 32 that arrival time fluctuations for Ray ID +6 at the 800m sensor depth matches well with the mode 1 amplitude time series for DVLA. This highlights the connection between arrival time fluctuations and internal tide mode structure and also, gives credence to the foregone conclusion that the acoustic travel time fluctuations for this ray were affected by the semidiurnal component of the internal tide between DVLA and T1. However, the degree to which acoustic arrival time fluctuations are effected by the modal structure is a complicated puzzle, as can be seen in Figure 33, where there appears to be minimal connection with the mode 2 structure at T1. Comparison of modal structure to arrival time fluctuations is beyond the scope of this thesis but analysis of this topic may prove beneficial in future work.

To further analyze the Viterbi tracked ray arrivals during the spring and neap times, we needed to verify that the difference between the mean arrival times for each part of the cycle was statistically significant. Since the sample sizes and variances were different, a two-sided T-test was performed on each data set. An alpha of 0.01 was used. It was determined the difference between the means of the spring and neap time periods for all of the tracked rays, proved to be, with 99% confidence, statistically significant. The next step was to calculate the VAR of the arrival time fluctuations for each tracked ray during the spring and neap cycle (Figure 34).
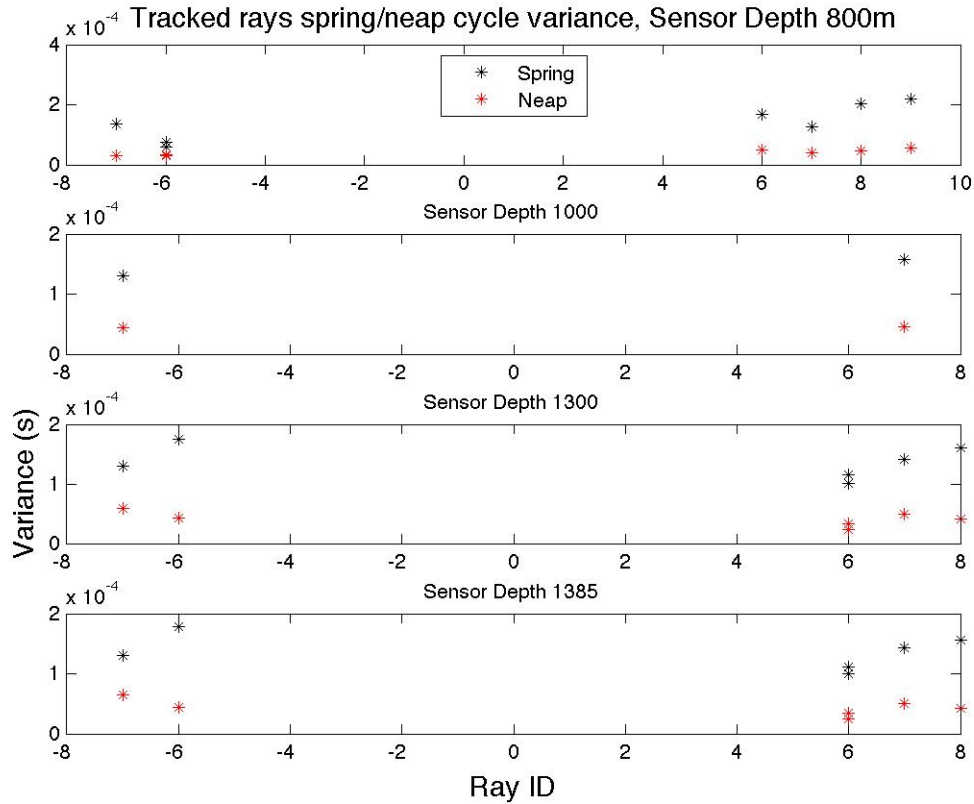

Figure 34. Tidal range variance for all tracked rays at each sensor depth.

The variances in Figure 34 show that every ray we tracked was affected by the spring/neap cycle. This is significant because it shows that arrival time

fluctuations are directly tied to internal tidal amplitude fluctuations. For larger tidal amplitudes, you would expect to see more variability in arrival time fluctuations.

C. FUTURE WORK

Compared to the follow-on 2010-2011 NPAL experiment the data collected during the NPAL pilot study were limited in scope, and data resolution. The NPAL 2010-2011 study was conducted over the course of a year, and had greater time and depth resolution than the 2009 pilot study.

The data from the 2010-2011 experiment should be used to track the timefronts across all depths, and study the seasonal low frequency variability due to eddies and other mesoscale disturbances. The data should also be used to resolve more tides. A comparison of tracked peaks with the internal tide model for multiple spring/neap cycles can then be used to provide a more comprehensive understanding of how evolving tides affect acoustic travel times (Worcester, 2008).

A more accurate modal analysis can be conducted on the 2010-2011 data with the increased number of sensors distributed throughout the water column, requiring less data extrapolation for depth than the 2009 data. The modal analysis conducted within this thesis showed that modes higher than mode 1 possessed a significant amount of energy, contrary to previous conclusions. The data from the NPAL 2010-2011 study should be used to compare acoustical data for higher internal tide modes in this complex region, to better understand the effect of the higher modes on acoustic propagation.

Finally, data from the DVLA and the other moorings should be used to determine if there is a difference in the travel time variation depending on the bearing angle from the source to the receiver. This will require a comparison of the phase changes for acoustic signals propagating in reciprocal directions.

LIST OF REFERENCES

Bell, T. H., 1975: Topographically generated internal waves in the open sea. *Journal of Geophysical Research*, **80(3)**. 320–327.

Colosi, J.A., L.J. Van Uffelen, B.D. Cornuelle, M.A. Dzieciuch, P.F. Worcester, B.D. Dushaw, and S.R. Ramp, 2012: Observations of sound-speed fluctuations in the western Philippine Sea in the spring of 2009. Preprint submission, *Journal of the Acoustical Society of America*.

Colosi, J.A., J. Xu, P.F. Worcester, M.A. Dzieciuch, B.M. Howe, and J.A. Mercer, 2009: Temporal and vertical scales of acoustic fluctuations for 75-Hz, broadband transmissions to 87-km range in the eastern North Pacific Ocean. *Journal of the Acoustical Society of America*, **126(3)**. 1069-1083.

Flatte, S.M., 1983: Wave propagation through random media: Contributions from ocean acoustics. *Proceedings of the IEEE*, **71(11)**. 1267-1294.

Garrett, C., and E. Kunze, 2007: Internal tide generation in the deep ocean. *Annual Review of Fluid Mechanics*, **39**. 57-58. [Available online at web.uvic.ca/~opg/people/garrett/abstracts/AR07pub.pdf]

Girton, J.B., B.S. Chinn, and M.H. Alford, 2011: Internal wave climates of the Philippine Seas. *Oceanography*, **24(1)**.100–111.

Hendershott, M., 1980: Long waves and ocean tides. *Evolution of Physical Oceanography*, B.A. Warren, and C. Wunsch, Ed., Massachusetts Institute of Technology, 292-341.

Jensen, F.B., W.A. Kuperman, M.B. Porter, and H. Schmidt, 1994: *Computational Ocean Acoustics*. 1st ed. American Institute of Physics, 595pp.

Kerry, C.G., B.S Powell, and G.S. Carter, 2013: Effects of remote generation sites on model estimates of M_2 internal tides in the Philipine Sea. *Journal of Physical Oceanography*, **43**. 187-204.

Levine, M.D., 2002: A modification of the Garrett-Munk internal wave spectrum. *Journal of Physical Oceanography*, **32**. 3166-3181.

Mitra, S., 2010: *Digital Signal Processing*. McGraw-Hill, 940pp.

Munk, W., 1981: Internal waves and small scale processes. *Evolution of Physical Oceanography*, B.A. Warren, and C. Wunsch, Ed., Massachusetts Institute of Technology, 264-291.

Munk, W., P. Worcester, and C. Wunsch, 2009: *Ocean Acoustic Tomography*. Cambridge University Press, 447pp.

Stewart, R.H., cited 2013: *Introduction to Physical Oceanography*. [Available online at http://oceanworld.tamu.edu/resources/ocng_textbook/contents.html]

Sutherland, B. R., G. O. Hughes, S. B. Dalziel, and P. F. Linden, 2000: Internal waves revisited. *Dynamics of Atmospheres and Oceans*, **31**. 209-232.

Worcester, P. F., and R. C. Spindel, (2005): North Pacific Acoustic Laboratory. *Journal of the Acoustical Society of America*, **117**. 1499–1510.

Worcester, P., 2008: NPAL Philippine Sea Experiment Plans. Preprint, *Office of Naval Research,* Codes: 321OA and 321US, [Available online at ftp://ftp.soest.hawaii.edu/bhowe/outgoing/Phil_Sea/plans_PhilSea.081017.doc]

INITIAL DISTRIBUTION LIST

1. Defense Technical Information Center
   Ft. Belvoir, Virginia

2. Dudley Knox Library
   Naval Postgraduate School
   Monterey, California